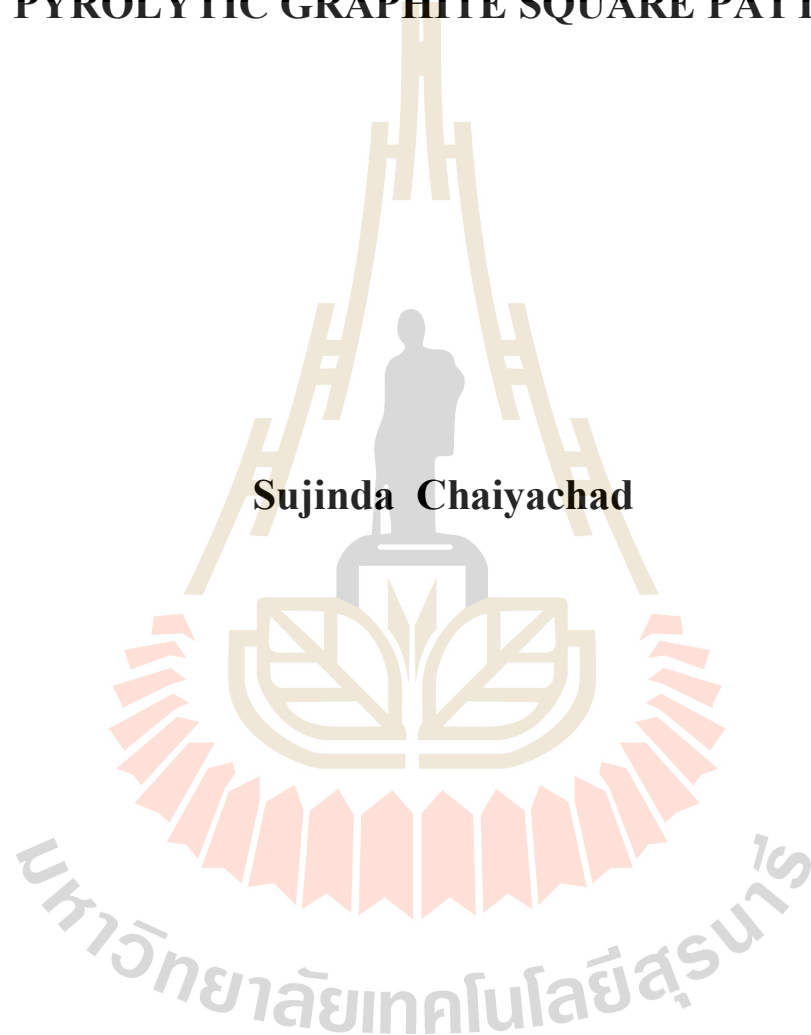


**ELECTRONIC STRUCTURE OF NANOSCALE
CRYSTALLINE HIGHLY ORIENTED
PYROLYTIC GRAPHITE SQUARE PATTERN**



Sujinda Chaiyachad

A Thesis Submitted in Partial Fulfillment of the Requirements for the

Degree of Doctor of Philosophy in Physics

Suranaree University of Technology

Academic Year 2020

โครงสร้างทางอิเล็กทรอนิกส์ของผลึกระดับนาโนรูปสี่เหลี่ยม
ของไฟโรไลต์กราฟไฟท์ที่มีความเข้มข้นสูง

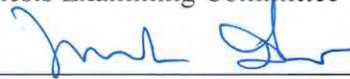


วิทยานิพนธ์นี้เป็นส่วนหนึ่งของการศึกษาตามหลักสูตรปริญญาวิทยาศาสตรดุษฎีบัณฑิต
สาขาวิชาฟิสิกส์
มหาวิทยาลัยเทคโนโลยีสุรนารี
ปีการศึกษา 2563

**ELECTRONIC STRUCTURE OF NANOSCALE CRYSTALLINE
HIGHLY ORIENTED PYROLYTIC GRAPHITE SQUARE
PATTERN**

Suranaree University of Technology has approved this thesis submitted in partial fulfillment of the requirements for the Degree of Doctor of Philosophy.

Thesis Examining Committee



(Asst. Prof. Dr. Panomsak Meemon)

Chairperson



(Assoc. Prof. Dr. Worawat Meevasana)

Member (Thesis Advisor)



(Assoc. Prof. Dr. Sirichok Jungthawan)

Member



(Assoc. Prof. Dr. Pisith Singjai)

Member



(Dr. Narong Chanlek)

Member



(Assoc. Prof. Dr. Chatchai Jothityangkoon)

Vice Rector for Academic Affairs

and Quality Assurance

(Prof. Dr. Santi Maensiri)

Dean of Institute of Science

ศุจินดา ไชยชาติ : โครงสร้างทางอิเล็กทรอนิกส์ของผลึกระดับนาโนรูปสี่เหลี่ยมของไฟโรไลติกกราฟไฟท์ที่มีความเข้มข้นสูง (ELECTRONIC STRUCTURE OF NANOSCALE CRYSTALLINE HIGHLY ORIENTED PYROLYTIC GRAPHITE SQUARE PATTERN). อาจารย์ที่ปรึกษา : รองศาสตราจารย์ ดร.วรวัดน์ มีวาสนา, 86 หน้า.

วัสดุที่มีพื้นฐานเป็นคาร์บอนสองมิติ เช่น กราฟีนและกราฟไฟท์ได้แสดงให้เห็นถึงศักยภาพที่ดีสำหรับอุปกรณ์อิเล็กทรอนิกส์ในอนาคต คุณสมบัติที่สนใจของกราฟีนซึ่งมีความสำคัญต่ออุปกรณ์ออปโตอิเล็กทรอนิกส์คือการทวีคูณของประจุตัวนำซึ่งหมายความว่าโฟตอนตัวเดียวจะสร้างประจุตัวนำได้มากกว่าหนึ่งตัวโดยกระบวนการ Auger อย่างไรก็ตามข้อเสียอย่างหนึ่งที่จะเป็นประโยชน์ในฐานะวัสดุอิเล็กทรอนิกส์คือการขาดช่องว่างพลังงาน ในงานนี้ได้ทำการศึกษาโครงสร้างทางอิเล็กทรอนิกส์ของไฟโรไลติกกราฟไฟท์ที่มีผลึกระดับนาโน (nano HOPG) ที่เตรียมโดยลำแสงไอออนที่พุ่งออกมา (Focused ion beam) รูปร่างของไฟโรไลติกกราฟไฟท์ที่มีผลึกระดับนาโนมีลักษณะเป็นเกาะสี่เหลี่ยมบนพื้นผิวครอบคลุมพื้นที่ 100 x 100 ตารางไมโครเมตร ยิ่งไปกว่านั้นไฟโรไลติกกราฟไฟท์ชั้นสูงที่มีผลึกระดับนาโนยังคงอยู่ในแนวผลึกเดียวกันกับพื้นผิวเดิม ด้วยการใช้เทคนิคโฟโตมิซชันแบบแยกแยะเชิงมุม (ARPES) สามารถพบช่องว่างพลังงานของไฟโรไลติกกราฟไฟท์ที่มีผลึกระดับนาโนประมาณ 90 มิลลิอิเล็กตรอน โวลต์

เพื่อพิสูจน์การเปิดช่องว่างพลังงานนั้นเกิดได้อย่างไร เทคนิครามานสเปกโทรสโกปีและการคำนวณทางทฤษฎีโดยใช้ทฤษฎีฟังก์ชันความหนาแน่นถูกนำมาใช้ในการอธิบายด้วย สเปกตรัมของเทคนิครามานสเปกโทรสโกปีของไฟโรไลติกกราฟไฟท์ที่มีผลึกระดับนาโน เผยให้เห็นการเปลี่ยนแปลงของจุดยอดของโหมดการสั่นสองมิติในทิศทางที่มีความถี่น้อยลงอย่างมีนัยสำคัญเมื่อเทียบกับพื้นผิวของไฟโรไลติกกราฟไฟท์ การเปลี่ยนแปลงนี้อาจมาจากการขยายตัวของวงแหวนหกเหลี่ยมคาร์บอนซึ่งเรียกว่าความเครียดแรงดึง ผลการคำนวณทางทฤษฎีโดยใช้ทฤษฎีฟังก์ชันความหนาแน่นแสดงให้เห็นถึงความเป็นไปได้ของการเปิดช่องว่างพลังงานที่มาจากความเครียดแรงดึงซึ่งค่อนข้างสอดคล้องกับผลการทดลอง การค้นพบนี้แสดงให้เห็นถึงวิธีการใหม่ในการสร้างและควบคุมช่องว่างพลังงาน ของวัสดุที่มีพื้นฐานเป็นคาร์บอนสองมิติในพื้นที่ขนาดใหญ่

สาขาวิชาฟิสิกส์
ปีการศึกษา 2563

ลายมือชื่อนักศึกษา ศุจินดา ไชยชาติ
ลายมือชื่ออาจารย์ที่ปรึกษา ดร.วรวัดน์ มีวาสนา

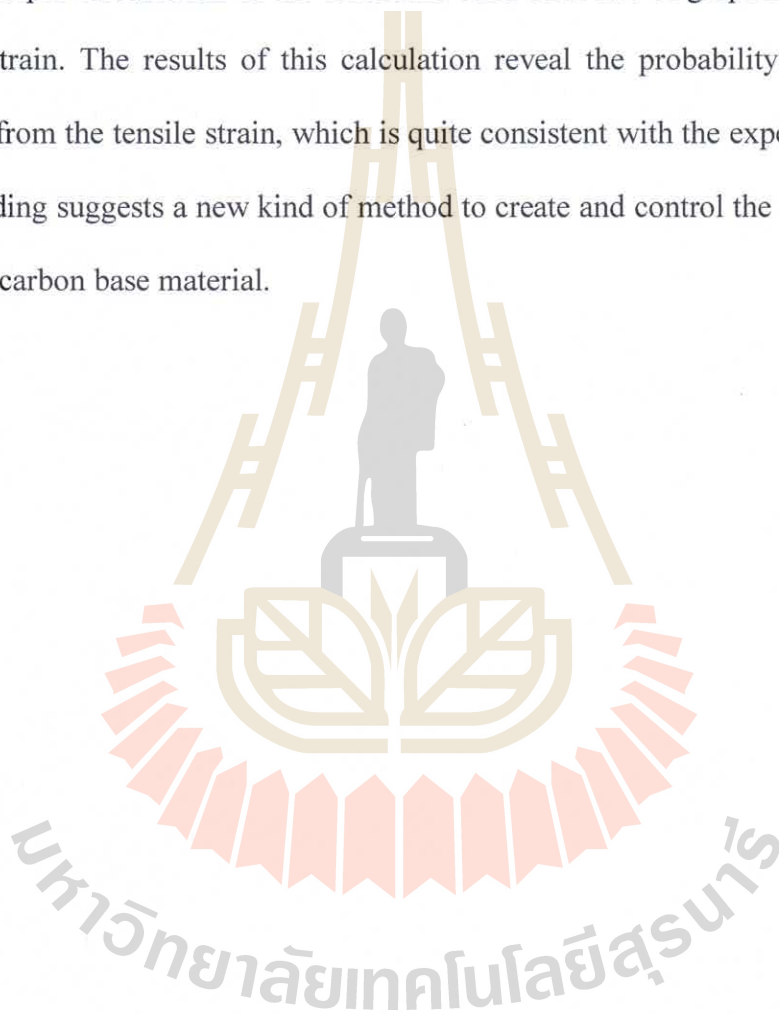
SUJINDA CHAIYACHAD : ELECTRONIC STRUCTURE OF NANO-
SCALE CRYSTALLINE HIGHLY ORIENTED PYROLYTIC GRAPHITE
SQUARE PATTERN: ASSOC. PROF. WORAWAT MEEVASANA, Ph.D.
86 PP.

LAYERED MATERIALS/BANDGAP OPENING/NANO PATTERN/FOCUSED
ION BEAM

Two-dimensional carbon-base materials such as graphene and graphite have shown great potential for next-generation electronic devices. The interesting property of graphene, which is important to optoelectronic devices, is carrier multiplication. That means a single photon generates charge carriers more than one by the Auger process. However, one of the disadvantages to being useful as an electronic material is the lack of bandgap. In this work, the electronic structure of nano-scale crystalline highly oriented pyrolytic graphite (HOPG) (one of the two-dimensional carbon-base materials) that was prepared by ion beam sputtered was investigated. The shape of nano HOPGs is a square island on a substrate cover area of $100 \times 100 \mu\text{m}^2$. Moreover, the array of nano HOPGs will still be in the same crystalline orientation as the original substrate. By using angle resolved photoemission spectroscopy (ARPES), the energy gap of nano HOPG was observed. The symmetrized ARPES spectrum of nanoscale HOPG revealed the gap opening of approximately 90 meV.

To prove how the opening of the energy gap occurred, Raman spectroscopy and theoretical computation using density function theory were also used in the explanations. A look at nanoscale HOPG shows that the peak position of the 2D mode

is a lot more redshifted than it is on the surface of the HOPG refers to the decreasing frequency of the 2D mode. There is a possibility that this redshift may come from the expansion of the carbon hexagonal ring, which is called tensile strain. In order to figure out how strain changes the electronic structure of graphene-based materials, we did first-principle calculations of the electronic band structure of graphene under a single tensile strain. The results of this calculation reveal the probability of gap opening coming from the tensile strain, which is quite consistent with the experimental results. This finding suggests a new kind of method to create and control the bandgap of large area 2D carbon base material.



School of Physics

Academic Year 2020

Student's Signature Sujinda

Advisor's Signature Oran

ACKNOWLEDGMENT

This thesis could not be completed without the help and support of many people. First and foremost, I am grateful to my advisor, Assoc. Prof. Dr. Worawat Meevasana. It is my luck that I have the opportunity to work under his supervision. all the time in his PhD studies. I had so much fun and felt like the luckiest student under his supervision, as he was a very good mentor with his kindness, dedication, and encouragement. I am grateful for what he has given me, such as the opportunity to conduct an experiment in the United States and learn from the best facilities in the world. Thus, I explored the wider world. With his understanding and patience, he always pushes me with a good attitude and scientific ideas to make me better. I will never regret what I have learned so far.

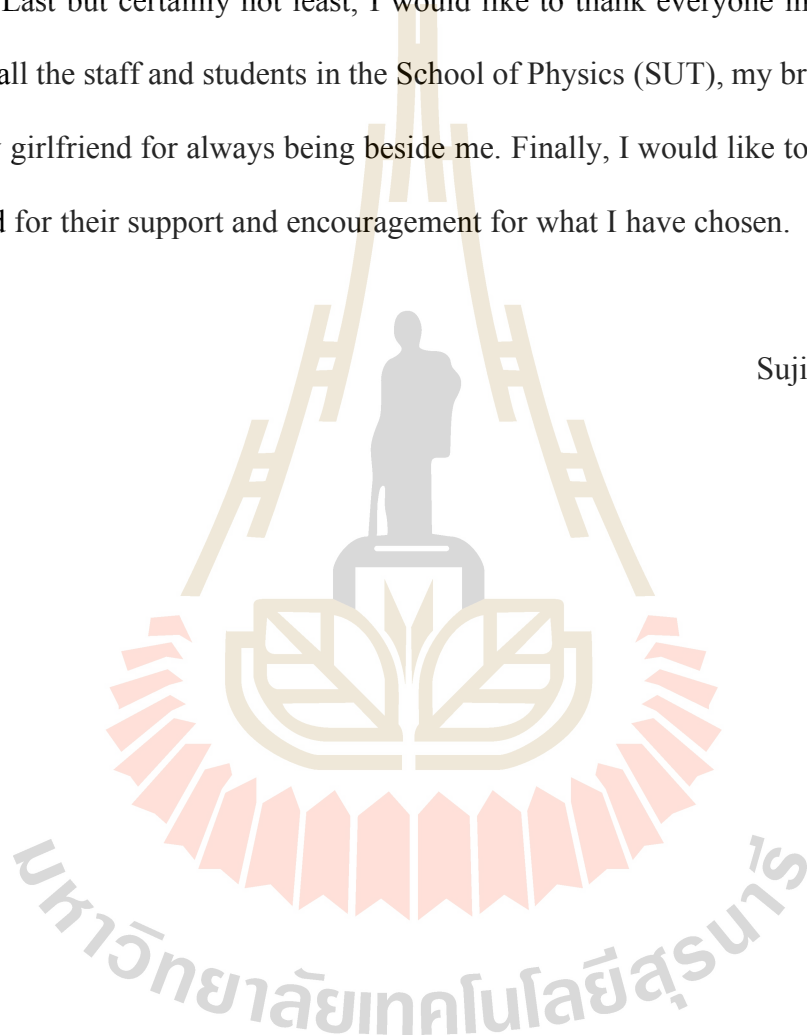
I would like to thank Dr. Ittipol Fongkaew and Mr. Sirisak Singesen for the calculation results that helped make this work perfect. They helped me design a computational model to get results consistent with my experiment.

For my defense, I would like to acknowledge Asst. Prof. Dr. Panomsak Meemon, Assoc. Prof. Dr. Sirichok Jungthawan, Assoc. Prof. Dr. Pisith Singjai, and Dr. Narong Chanlek, members of the thesis defense committee, for giving their valuable time and guiding good research aspects for my defense.

Importantly, I would like to acknowledge the Thai government for their support through the Development and Promotion of Science and Technology Talent Project (DPST) for financial support since my bachelor's degree.

Last but certainly not least, I would like to thank everyone in the Meevasana group, all the staff and students in the School of Physics (SUT), my brother, my sister, and my girlfriend for always being beside me. Finally, I would like to thank my mom and dad for their support and encouragement for what I have chosen.

Sujinda Chaiyachad



CONTENT

	Page
ABSTRACT IN THAI	I
ABSTRACT IN ENGLISHII
ACKNOWLEDGMENTS	IV
CONTENTS	VI
LIST OF FIGURES	XIV
CHAPTER	
I INTRODUCTION	1
1.1 Motivation	1
1.2 Objectives of research	2
1.3 Outline of thesis	2
II THEORY AND LITERATURE REVIEWS	4
2.1 Photoelectric effect	4
2.2 Photoemission spectroscopy	5
2.2.1 Three-step model	6
2.2.2 One-step model	7
2.3 Angle-resolved photoemission spectroscopy	9
2.4 Raman spectroscopy	12
2.5 Engineering of electronic structure of layered material	14
2.5.1 Electric field	19

CONTENTS (Continued)

	Page
2.5.2 Strain	22
2.5.3 Quantum confinement effect.....	24
2.5.4 Edge.....	28
2.5.5 Disorders in graphene structure.....	29
2.6 Nano patterning for devices fabrication	30
III MATERIALS AND METHODOLOGY	34
3.1 Layered material.....	34
3.1.1 Graphene.....	34
3.1.2 Highly oriented pyrolytic graphite.....	37
3.1.3 Transition metal dichalcogenides	39
3.2 Nano-pattern preparation.....	40
3.2.1 Focused ion beam.....	40
3.2.2 E-beam lithography.....	42
3.2.3 Nanoscale crystalline preparation.....	43
3.3 Angle resolved photoemission spectroscopy measurement.....	45
3.3.1 Nanoscale layered material preparation for ARPES measurement....	45
3.3.2 Electronic structure observation.....	46
3.3.3 Symmetrized spectrum	48
3.4 Raman spectroscopy.....	50
3.5 DFT calculation.....	51
IV RESULTS AND DISCUSSION	52
4.1 Morphology of nanoscale crystalline layered materials.....	52

CONTENTS (Continued)

	Page
4.2 Electronic structure of nano scale crystalline layered materials.....	56
4.3 Raman spectroscopy observation.....	62
4.4 Energy gap opening discussion.....	65
V CONCLUSIONS	71
5.1 Conclusions.....	71
5.2 Future direction.....	73
REFERENCES	74
CURRICULUM VITAE	85



LIST OF FIGURES

Figure	Page
2.1 Photoelectric phenomena for simple explanation.....	5
2.2 Illustration of three-step and one-step model crucially use for describing the possible photoemission process	8
2.3 Schematic illustration of ARPES system, consisting of incident photon light, sample and analyzer	10
2.4 A basic diagrammatic representation of light scattering processes using single molecule: Rayleigh scattering (blue) and anti-Stokes Raman scattering (red).....	12
2.5 a) Comparison of Raman spectra of bulk graphite and graphene at 514 nm. b) The evolution of the 514 nm spectra as the number of layers increases.....	14
2.6 a), b) Valence band measured along the $\Gamma-\bar{K}$ direction for bulk and monolayer MoS ₂ and c) conduction band of monolayer MoS ₂	15
2.7 a) PL spectra for mono and bilayer MoS ₂ samples in the photon energy range from 1.3 to 2.2 eV. b) Normalized PL spectra by the intensity of peak A of thin layers of MoS ₂ for N=1–6. c) Bandgap of thin layers of MoS ₂	16
2.8 Carrier multiplication (CM) process	17
2.9 a) The conductivity of graphene as a function of gate voltage measured at 10 K. b) Charge carrier density n_s and mobility μ of graphene as a function of gate voltage.....	20

LIST OF FIGURES (Continued)

Figure	Page
2.10 Evolution of gap closing and reopening by changing the doping level by potassium adsorption.....	21
2.11 a) Schematic of electric field that was applied in BLG and bandgap opening. b) Experimental results (red squares) are contrasted to theoretical predictions derived from self-consistent tight-binding calculations (black trace), ab initio density functional calculations (red trace), and unscreened tight-binding calculations (red trace) (blue dashed trace).....	21
2.12 a) The Raman spectra that are taken from the 2D band SLG. b) and c) Calculated band structure of unstrained and 1% tensile strained graphene	23
2.13 a) The band structure of single layer graphene at the K point under zigzag strain. b) The band structure of bilayer graphene at the K point when applied to a zigzag strain.....	23
2.14 a) Scheme of the cross section of the flexible substrate before and after bending it. b) Scheme of the approach to apply uniaxial tensile strain by elongating an elastic substrate. c) Schematic diagram of the mechanical deformation of a piezoelectric material when an electric field is applied. d) Schematic diagram of the process to strain atomically thin materials by using substrates with strong adhesion and very large thermal expansion coefficient. e) Schematic diagram of the fabrication process of wrinkled nanolayers.....	24
2.15 Bandgap difference of nanoparticle and bulk material	26

LIST OF FIGURES (Continued)

Figure	Page
2.16 a) Calculated emission wavelength (nm) using TDDFT method b) The bandgap of graphene dots (benzene ring) calculated based on DFT	26
2.17 Optical properties of the GQDs	27
2.18 The red line are a) zigzag edge of graphene nano ribbon (GNR), b) arm-chair edge of graphene nano ribbon and c) arbitrary edge of graphene nano ribbon	28
2.19 a) Scanning electron microscopy image of diamond nanopillars fabricated on a (111)-oriented single-crystalline diamond sample. b) Confocal fluorescence image of an array of diamond nanopillars	30
2.20 a) Top-view SEM image of a square array of silicon nanoscatterers on a sapphire cover slide, made by SCIL. b) SEM image of a cross section of the silicon nanoscatterers on sapphire made using focused ion beam milling ...	31
2.21 a) A typical graphene micro-ribbon arrangement from the top. b) A typical device with a graphene micro ribbon array on a Si/SiO ₂ substrate from the side. c) AFM image of a graphene micro-ribbon array sample with a 4 μm ribbon width and a 1:1 ratio of ribbon to gap width	32
2.22 a) The investigated device geometry is represented schematically. b) Optical microscope taken from the top of a device with an array period(Λ) = 6 μm. c) Calculated resonance frequency of grating-coupled GPPs, plotted as a function of carrier density N for different values of Λ	32

LIST OF FIGURES (Continued)

Figure	Page
3.1 a) Sigma and pi bonds in graphene. b) Electronic structure of graphene. Valence and conduction bands meet at the six vertices of the hexagonal Brillouin zone and form linearly dispersing Dirac cones.....	35
3.2 a) Auger recombination (AR) b) Inverse Auger recombination or impact ionization (II).....	36
3.3 a) Fermi energy intensity map. The hexagonal Brillouin zone dashed lines and Fermi surface shaded circles expected for single crystalline graphite are drawn schematically. b) Intensity map vs binding energy and in-plane momentum along the solid line in a taken at 60 eV photon energy. c) Second derivative of raw data in b with respect to energy.....	38
3.4 a) Side-view of atomic structure of transition metal dichalcogenides (TMD) where M represents a transition metal and X represents a chalcogen. b) Top-view of atomic structure of transition metal dichalcogenides (TMD).....	39
3.5 Principle of FIB a) imaging, b) milling and c) deposition	41
3.6 Schematic representation of the lithographic process.....	42
3.7 Field Emission Scanning Electron Microscope (FE-SEM) at the center for scientific and technology equipment, Suranaree University of Technology.....	44
3.8 a) array pattern of 50 x 50 lines as an ion beam mask for nano pattern preparation. b) 4 masks on the surface of the sample surface	45
3.9 ARPES system at CASSIOPEE beamline.....	47
3.10 The combined spectrums of the case of there are no energy gap and there is energy gap	49

LIST OF FIGURES (Continued)

Figure	Page
3.11 SENTERRA II Dispersive Raman Microscope from Bruker Optics.....	50
4.1 Schematic of nano-scale HOPG on HOPG substrate.....	53
4.2 SEM picture of nanoscale crystalline on a HOPG substrate as prepared by using a mask of 100 lines x 100 lines a) 2kx and b) 5kx of magnification.....	53
4.3 SEM picture of nanoscale crystalline on a HOPG substrate as prepared by using a mask of 50 lines x 50 lines	55
4.4 a) Electronic structure of highly oriented pyrolytic graphite (HOPG) consist of Femi surface map of HOPG. b) Band dispersion along red arrow in figure a) and insert figure is band dispersion near Fermi level in black solid box.....	56
4.5 a) and b) Band dispersion near Fermi level of HOPG which were evapo- rated Cs 0 minute and 5 minutes, respectively	57
4.6 Dirac cone (a. and b.) and spectral weight of nano HOPG and normal HOPG (c.). EDC spectrum of nano HOPG exhibit bandgap opening 0.285 eV and Dirac point of normal HOPG indicated by blue arrow and text.....	58
4.7 a) position mapping in 100 x 100 um per step and b) Symmetrization spectrums of EDCs at KF of ARPES spectrum of each position	59
4.8 a) and b) Symmetrized ARPES spectra of nanoscale crystalline HOPG with crystalline diameters of 500 nm and normal HOPG, respectively. c) EDC spectra across KF of nanoscale crystalline HOPG and normal HOPG. d) Symmetrized of c) that Fermi level is referenced with gold.....	60

LIST OF FIGURES (Continued)

Figure	Page
4.9 a) – d) ARPES spectra, e) – h) Symmetrized ARPES spectra, i) – l) Energy dispersion curve (EDC) spectra across k_F of ARPES spectra and m) – p) Symmetrized energy dispersion curve (EDC) spectra across k_F of ARPES spectra of nanoscale HOPG pattern, HOPG substrate, near nanoscale HOPG pattern, and Au respectively	61
4.10 Raman spectra of nanoscale HOPG pattern (blue), HOPG substrate (black), and near nanoscale HOPG pattern (red). Inset figure is zoom in D and G peak of nano HOPG Raman spectrum	63
4.11 2D mode Raman spectrum with two peaks of Lorentzian fitting and linear background	64
4.12 Bandgap of graphene quantum dots (GQDs) is compared to the bandgap of nano HOPG	66
4.13 a) 2D mode of Raman spectra of nanoscale HOPG pattern (blue), HOPG substrate (black), and near nanoscale HOPG pattern (red). b) Peak position of second peak of 2D mode Raman spectra of bulk and nanoscale crystalline HOPG	67
4.14 (a) The geometric structure of trilayer graphene. (b) Schematic of biaxial tensile strain with a same strain value along x- and y-direction. (c) The comparative energy gap of monolayer, trilayer graphene, and nano HOPG. The corresponding band structure of monolayer graphene with applied 1.1% strain (d), trilayer graphene with no strain (e), and trilayer graphene with applied 1.1% strain (f)	69

CHAPTER I

INTRODUCTION

In this chapter, the motivation for my thesis was presented as the first topic. Then, my thesis objectives were displayed in the second topic. The last topic in this chapter is the outline of my thesis.

1.1 Motivation

Two-dimensional materials, e.g., graphite/graphene and transition metal dichalcogenides (TMDs), are interesting materials because their electronic properties, such as band gap, will be changed by the number of layer variations. Because of this property, they are very promising for a wide range of applications, including chemical and biosensors, energy storage, and optoelectronic devices such as solar cells. For solar cell applications, the band gap of materials is very important. It needs to be matched with the solar spectrum in the NIR to UV range. The bandgap of TMDs has been observed in this range. Graphene has no bandgap, which is its main disadvantage. However, its band gap can be opened by applying strain (Ni et al., 2008 and Cocco et al., 2010) electric field (Castro et al., 2007) and quantum confinement effect (Sk et al., 2014; Eda et al., 2010; Peng et al., 2012 and Kim Sung et al., 2012). Moreover, graphene has an outstanding property for optoelectronic devices: the carrier multiplication (CM) property, which can improve the light conversion efficiency of the solar cell. Therefore, it is very important to understand and find a new way to tune the electronic structures of these layered materials. The electronic properties and

mechanism of bandgap engineering of these materials are essential for solar cell application. Many researchers have used layered materials to make solar cells, but the efficiency is still low when compared with silicon solar cells. Moreover, silicon solar cells that are made from monocrystalline silicon are more efficient than polycrystalline. It shows that a monocrystalline is more efficient as a device than a polycrystalline. Therefore, in this work, we would like to study the electronic structure, especially bandgap engineering, of crystalline layered materials by cutting them to the nanoscale. The nanoscale crystalline layered materials such as graphene and TMDs will be prepared by the focused ion beam (FIB) technique. Their electronic structures will be investigated and studied using photoemission spectroscopy and microscopy.

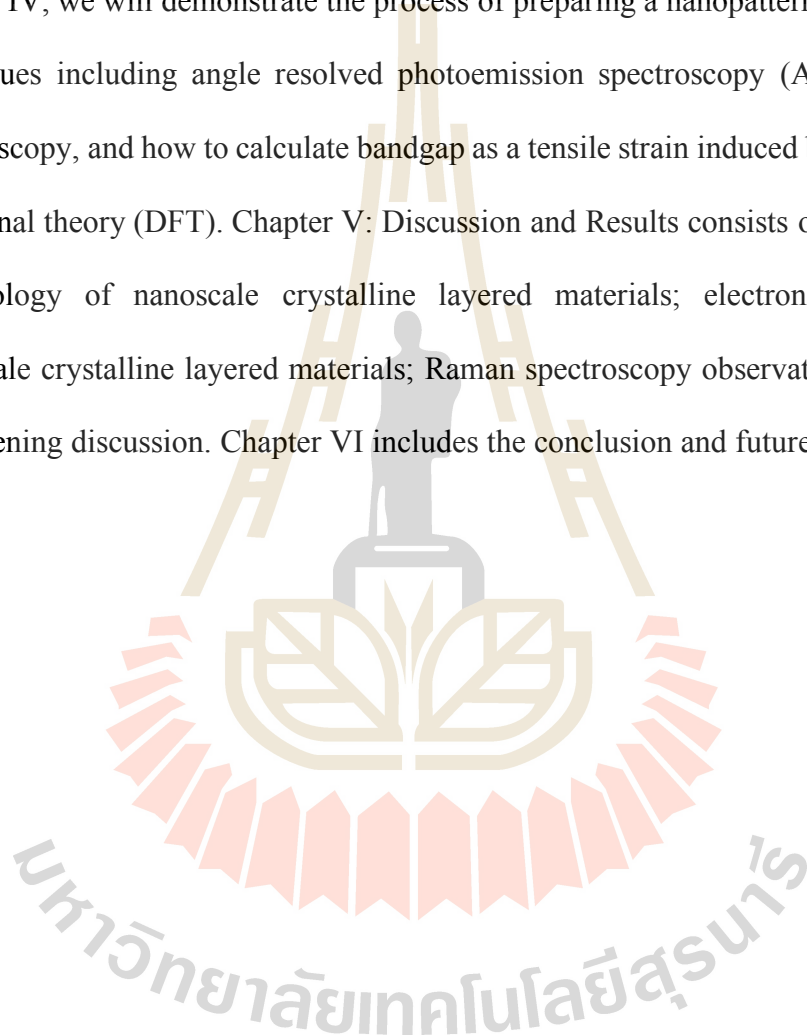
1.2 Objectives of research

1. To prepare the nanoscale single crystal graphite-base material
2. To study the electronic structure of the single crystal graphite-base material by angle resolved photoemission spectroscopy

1.3 Outline of thesis

The thesis is separated into 6 chapters. Chapter I is the introduction part, which includes the motivation, approach of the electronic structure engineering of bulk and nanoscale crystalline layered materials studies, and thesis objective. Chapter II presents photoemission spectroscopy, which is the main technique for electronic structure observation. This chapter consists of the introduction of photoemission spectroscopy with the original view of the photoelectric effect. Then, the technique that was called

"ARPES" is presented. The additional sections on photoemission spectroscopy include energy gap analysis, PEEM, and sample preparation for ARPES measurement. Other related theoretical aspects consist of layered material details, nano pattern preparation, Raman spectroscopy, and engineering of the electronic structure of layered material. In chapter IV, we will demonstrate the process of preparing a nanopattern and measuring techniques including angle resolved photoemission spectroscopy (ARPES), Raman spectroscopy, and how to calculate bandgap as a tensile strain induced by using density functional theory (DFT). Chapter V: Discussion and Results consists of the following: morphology of nanoscale crystalline layered materials; electronic structure of nanoscale crystalline layered materials; Raman spectroscopy observation; and energy gap opening discussion. Chapter VI includes the conclusion and future directions.



CHAPTER II

THEORY AND LITERATURE REVIEWS

Photoemission spectroscopy is a key method used in this study for observing electronic structures. As a result, this chapter established the theoretical basis for photoemission. This chapter begins with the principle of the photoelectric effect, followed by the photoemission spectroscopy theory. Then, the technique that was called "ARPES" is presented. Raman spectroscopy was also presented later. Because we are interested in the electronic structure of nanoscale crystalline layered materials, this chapter discusses the engineering of the electronic structure of layered materials and nanopatterning for device manufacturing.

2.1 Photoelectric effect

The photoelectric effect, which is electron leave from a material phenomenon, was discovered by Hertz in 1887 (Hertz, 1887). In 1905, Einstein explained that Photoelectric phenomenon is a quantum characteristic of light. Photoelectric effect is directly related to work and function, which is an intrinsic property of a material. Figure 2.1 exhibits photoelectric phenomena. When a material is stimulated by photon with energy ($h\nu$) that has more energy than the material's work function (Φ). Electrons are kicked out from the surface of the material by kinetic energy (E_k) where their relation can be written as

$$E_k = h\nu - \Phi \quad (2.1)$$

Photoelectric effects are used in studies in condensed matter and solid-state physics to

analyze the properties of atoms, molecules of materials. The technique that applies this phenomenon is called photoemission spectroscopy.

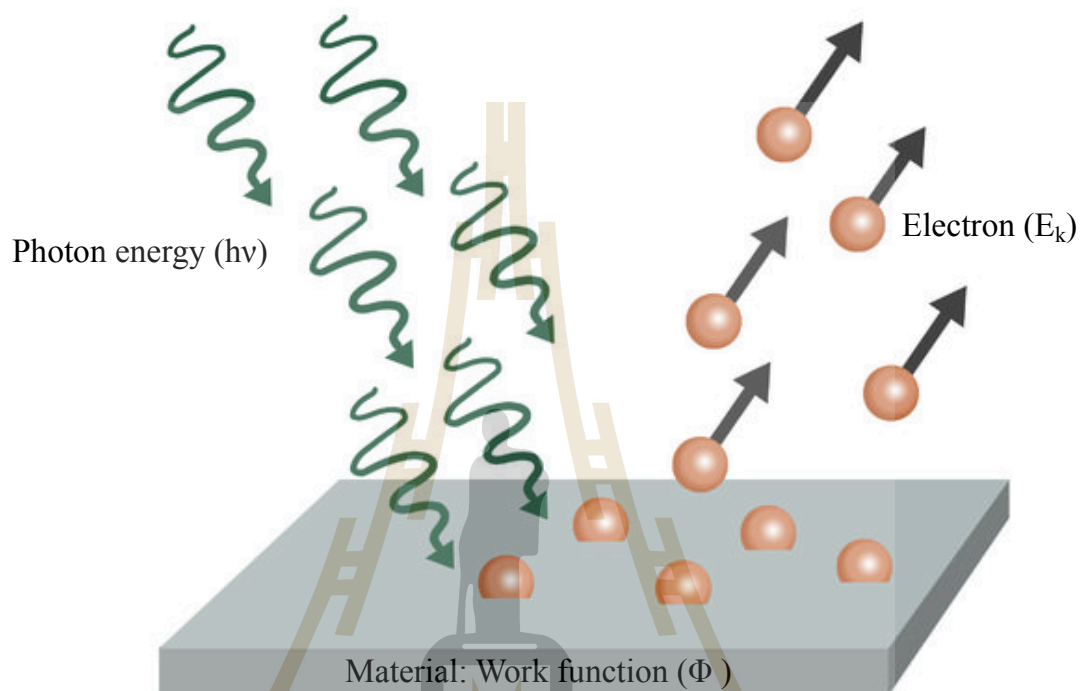


Figure 2.1 Photoelectric phenomena for simple explanation (Hertz, 1887).

2.2 Photoemission spectroscopy

Photoemission spectroscopy (PES) is the technique used to probe the electronic structure of the materials based on the photoelectric effect. PES is able to locate an electron that has escaped from its atomic structure by its kinetic energy. The kinetic energy of the ejected electrons is related to the binding energy (E_B) of the electrons in the atom as shown in the equation below.

$$E_k = h\nu - \Phi_A - E_B \quad (2.2)$$

Normally, the work function of the analyzer (Φ_A) is more than the work function of

material. Therefore, Φ_A is normally considered to be the reference functionality associated with the Fermi level in all experiments. (using the same analyzer). Photoemission mechanism is described by three-step model and the one-step model.

2.2.1 Three-step model

The three-step model is often used to explain the photoemission process in its simplest form. Figure 2.2 (left) depicts the three essential processes and an explanation of this approach. The photoelectron's photoexcitation, transportation, and escape are shown here.

I) Electron photoexcitation inside the sample

This process happens when a photon excites an occupied electronic state (initial state) to an unoccupied state. The photon is then adsorbed, resulting in the formation of an electron-hole pair within the crystal with the transition probability specified by the Fermi golden rule. This regulation will be discussed in more detail in the next section. Due to the low momentum of photons, the electron momentum is similarly unaltered in this state.

II) Photoelectron transport to the surface

This approach can be defined in terms of a mass-mean-free effective route for any material. This phrase refers to the likelihood that an excited electron may pass through a surface without being scattered. During this procedure, certain inelastic scattering electrons generate some unnecessary continuous background spectra, which are typically removed.

III) The photoelectron's escape into the vacuum

To escape from the surface, the excited electron needs energy greater than the work function of the materials. The momentum perpendicular to the surface is

not preserved in this process, since it depends on the excited energy and the sample surface. As a result, this step gives information on the likelihood of transmission out of the surface as a function of the excited energy and work function.

2.2.2 One-step model

The one-step model treats the whole photoemission process as a single step. The whole process may be summarized as follows: An excited electron moves from a Bloch starting state to a damped final state near the surface. This dampening condition of the electron ensures that the electron travels through the solid's surface with a short mean free path. In contrast to the three-step model, the one-step model combines the three artificial stages of the three-step model into a single cohesive process, as shown in Figure 2.2 (right). The photoemission process is corrected using Fermi's Golden Rule and appropriate functions for the starting and ending states. This is not an issue that can be addressed rigorously. The key to attempting the solution, however, is the simplification inherent in the sudden approximation, which is widely employed in many-body computations of photoemission spectra. This approximation works by assuming that there is no post-collision interaction between the photoelectron and the system and that there is no relaxation from the excitation. This approximation is adequate for photoelectrons with a reasonably large kinetic energy.

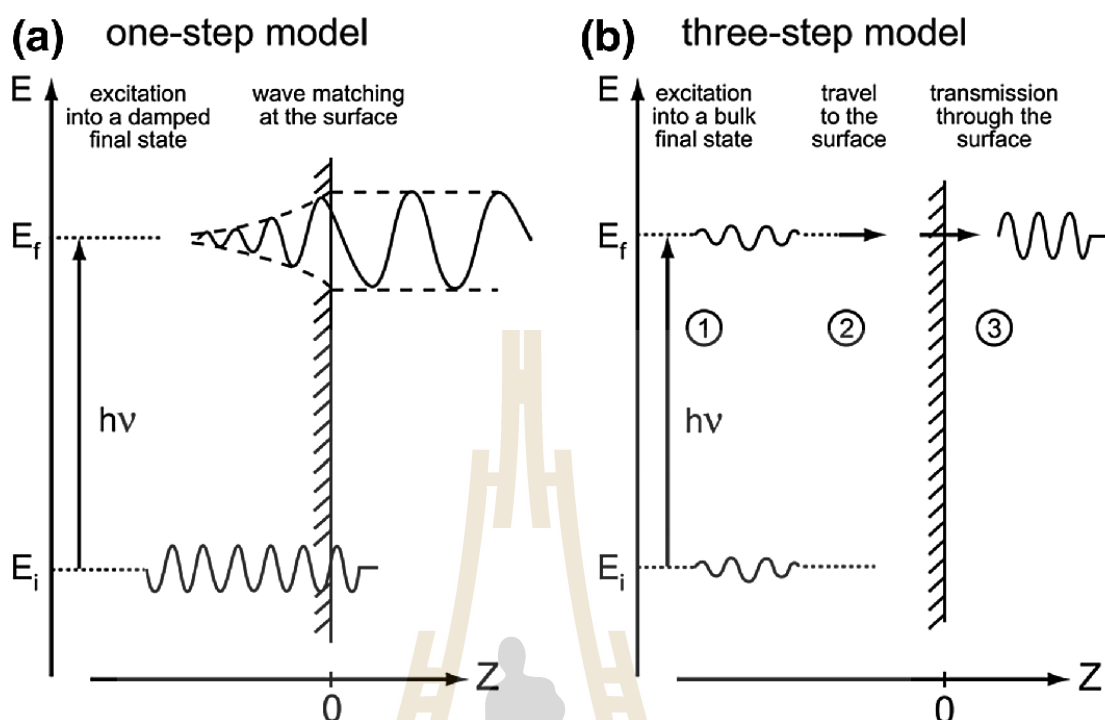


Figure 2.2 Illustration of three-step and one-step model crucially use for describing the possible photoemission process (Hu \ddot{u} fn \ddot{e} r, 1995).

The types of photoemission depend on excitation photon energy, such as X-ray or UV. X-ray Photo-Electron Spectroscopy (XPS), which uses X-rays as a photon light source, was developed by Kai Siegbahn starting in 1967. XPS is used to study the energy levels of atomic core electrons, mostly solids. Ultraviolet Photo Electron Spectroscopy (UPS) uses ultraviolet (UV) as a photon light source and is used to study valence and chemical bond energy levels, especially the bond nature of molecular orbitals. In condensation physics, the location of valence electrons results in interesting novel properties. Therefore, the determination of the position of valence electrons in both their energy and momentum is important. The technique that can be performed is Angle-resolved photoemission spectroscopy (ARPES).

2.3 Angle-resolved photoemission spectroscopy

Angle-resolved photoemission spectroscopy (ARPES) was used to observe electronic structure of materials. ARPES data can be obtained for both the energy (E) and the momentum (k) of the electron, thus obtaining detailed information about the bands dispersion and fermi surfaces. Regarding the photoelectric effect, the electrons with different E_k , resulting from excited by photon energy, were analyzed as a function of the angle (θ) of the analyzer. This angle (θ) related with the in-plane momentum ($k_{//}$) by this equation:

$$k_{//} = \sqrt{\frac{2m_e E_k}{\hbar^2}} \sin\theta \quad (2.3)$$

whereas m_e is effective mass of electron and \hbar is Planck constant. The results from ARPES measurement are expressed in photocurrent term ($I(E, k_x, k_y)$). We can gain information of in-plane dispersion of the occupied bands by tracing the peaks in the photocurrent. A plot of photocurrent for a fixed momentum is called “energy distribution curve (EDC)” while a plot of photocurrent with a fixed energy is called “momentum distribution curve (MDC)”. The out-of-plane or perpendicular momentum denoted as k_{\perp} , cannot be directly measured from ARPES because the k_{\perp} is large relative to the vacuum level.

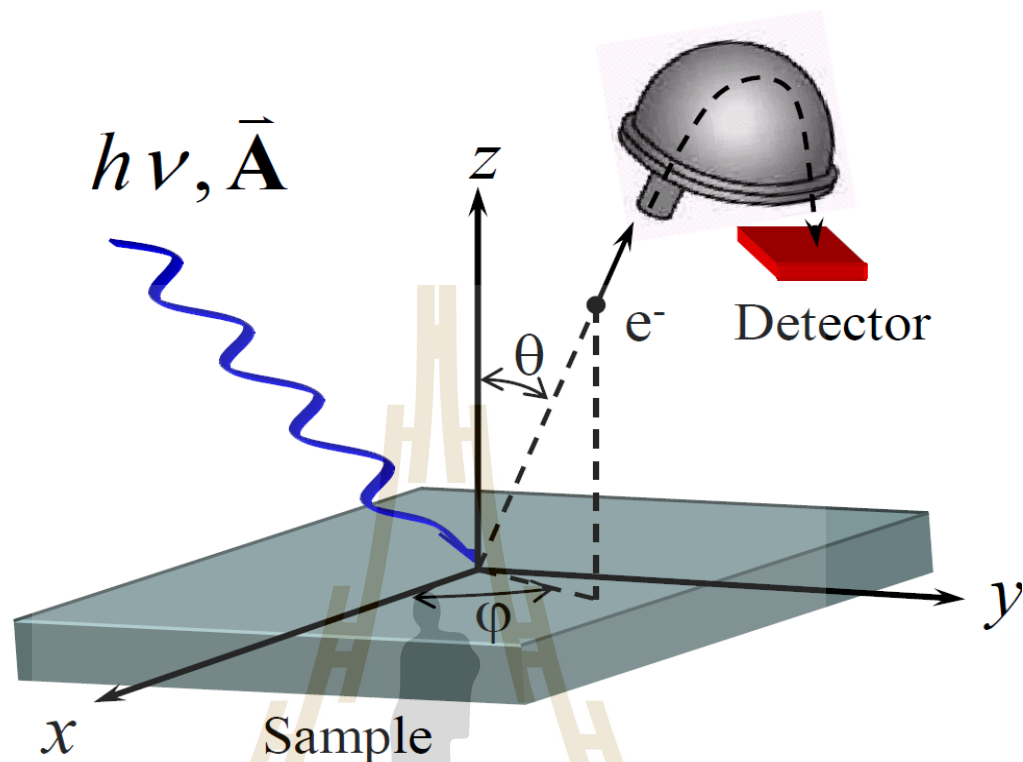


Figure 2.3 Schematic illustration of ARPES system, consisting of incident photon light, sample and analyzer.

The ARPES system, as shown in figure 2.3, was set up using synchrotron rays and a UV lamp as the light source. Most of the time, synchrotron radiation is used because the photon energy can be adjusted. Synchrotron light radiation is generated by electron acceleration and then travels through a bending magnet and is stored within the storage ring. The resulting light has a range of energy covering electromagnetic waves. In ARPES, multi-wavelength light passes through a sieve for wavelength selection, creating a monochromatic photon. Ultraviolet (UV) photon energy is typically used for surface-sensitive ARPES because of the average-free path of the typical atomic layers. To increase the desired photon flux output and spot size, a large number of inserts, such

as wigglers or undulators, are installed along the storage ring. ARPES measurements require high-resolution data acquisition for reliable experimental results. The resolution of the ARPES measurement depends on the intensity of the light source and the electron analyzer, which is the main component in the ARPES system. Moreover, the development of the two components in conjunction with sample cooling and sample manipulating provides a 10 meV energy resolution that can be used to detect many interesting physics phenomena. The electron analyzer is one of the major components of ARPES, consisting of an electrostatic lens, hemispherical deflector, entrance slit, exit slit, and electron detector. Firstly, the traditional hemispherical analyzer is discussed in order to understand the simple view of electron collection. The excited electrons from the sample are focused and retarded by the electrostatic lens at the entrance slit. This allows some electrons with the right kinetic energies within a narrow range centered at

$$E_{pass} = \frac{e\Delta V}{\frac{R_2 - R_1}{R_1} \frac{R_1}{R_2}} \quad (2.4)$$

These electrons which satisfy this equation can reach the exit slit and then the detector without colliding with the analyzer wall. Where ΔV is a potential difference, R_1 and R_2 are radius of two hemispheres. The energy resolution of measured electron can be calculated by

$$\Delta E_a = E_{pass} \left(\frac{d_w}{R_0} + \frac{\alpha^2}{4} \right) \quad (2.5)$$

where d_w is the width of the entrance slit, $R_0 = \frac{R_1 + R_2}{2}$, and α acceptance angle. The photoemission intensity can be recorded as a function of kinetic energy by scanning the electrostatic lens.

2.4 Raman spectroscopy

Raman spectroscopy is a spectroscopic technique that is primarily used to identify the vibrational modes of molecules, but it may also be used to examine rotational and other low-frequency modes of systems (Graves and Gardiner, 1989). Raman spectroscopy has been used in chemistry to create a structural fingerprint that may be used to identify molecules. Raman spectroscopy is based on the inelastic scattering of photons, commonly referred to as Raman scattering. Typically, monochromatic light is generated by a laser. When the laser light interacts with molecular vibrations, phonons, or other system excitations, the energy of the laser photons is pushed up or down. The energy shift that is the Raman shift provides information on the system's vibrational modes. Figure 2.4 illustrates the Raman scattering mechanism schematically.

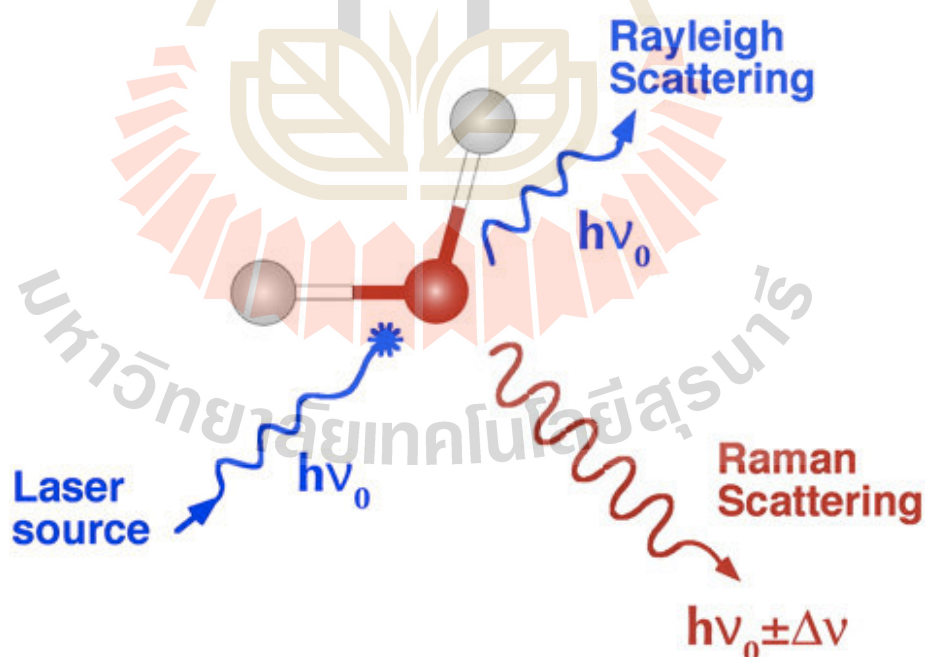


Figure 2.4 A basic diagrammatic representation of light scattering processes using a single molecule: Rayleigh scattering (blue) and anti-Stokes Raman scattering (red).

Raman shifts are often described in wavenumbers, which have inverse length units, since this value is linked to energy. The following formula may be used to convert between spectral wavelengths and Raman wavenumbers of shift:

$$\nabla\nu = \left(\frac{1}{\lambda_0} - \frac{1}{\lambda_1}\right) \quad (2.6)$$

where $\nabla\nu$ is the Raman shift expressed in wavenumber, λ_0 is the excitation wavelength, and λ_1 is the Raman spectrum wavelength. Raman spectroscopy is an extremely powerful technique for deciphering the intricate bonding structure of carbon-base materials. Raman spectroscopy has been essential in characterizing graphitic materials structurally and has developed into a useful tool for analyzing the behavior of electrons and phonons in graphene. Graphite's (graphene's) Raman spectrum is dominated by two Raman-allowed spectral characteristics. The G band is associated with the longitudinal optical (LO) phonon mode, which occurs about 1580 cm^{-1} , and the G' band (or 2D band) is an extremely powerful second-order dispersive Raman characteristic. Raman spectra of multilayer graphene exhibit a range of spectral widths and relative intensities for G to G', indicating interlayer interaction between graphene layers. For example, the graphene Raman spectrum can be differentiated from other spectra by the observation that the G' band is stronger than the G band, but the G' band is broader and weaker in multilayer graphene as shown in figure 2.5 (Ferrari et al., 2006).

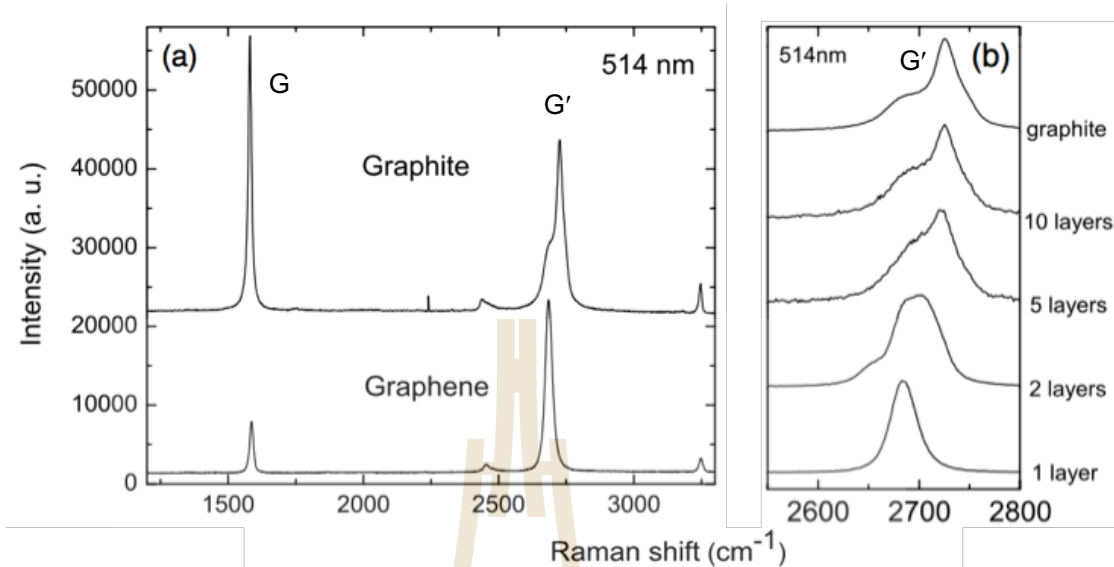


Figure 2.5 a) Comparison of the Raman spectra of bulk graphite and graphene at 514 nm. b) The evolution of the 514 nm spectra as the number of layers increases (Ferrari et al., 2006).

Graphene with a finite dimension involves irregularly shaped edges, stacking disorder between two layers, and atomic flaws inside the layer. The D-band characteristic arises at around 1350 cm^{-1} for such a disordered carbon. The ratio of D to G gives an excellent estimate of the in-plane crystallite size or the degree of disorder in the sample (Tuinstra and Koenig, 1970; Sato et al., 2006).

2.5 Engineering of electronic structure of layered material

Two-dimensional materials (2D materials or layered materials) are matter with a thickness of a few nanometers or less. Normally, the atomic structure of 2D materials consists of six atoms arranged in a hexagonal lattice in each layer. Electrons in the layered materials can move freely in the two-dimensional plane, but they are confined in the third direction. Because of their exceptional properties and application potential,

2D materials piqued the interest of many researchers (Novoselov et al., 2004; Novoselov et al., 2005; Zhang et al., 2005 and Berger et al., 2006). The layered materials are promising for a wide range of applications, including chemical and biosensors, energy storage, and optoelectronic devices. Electronic properties of layered materials can be changed by quantum confinement effects (QCE), and we especially investigated transition metal dichalcogenides (TMDs) and graphene. When materials transition from bulk to nano scale, QCE occurs. Some of the 2D materials are graphite, graphene, and transition metal dichalcogenides.

Transition metal dichalcogenides (TMDs) are semiconductors of the type MX_2 , where M is a transition metal atom (such as Mo or W) and X is a chalcogen atom (such as S, Se or Te). The TMDs exhibit a unique combination of atomic-scale thickness, direct bandgap, etc. The electronic properties of TMDs, such as band gap and work function, are transformed when their number of layers is altered. The bulk of TMDs have an indirect band gap, but they exhibit a direct band gap when they become monolayer (Eknapakul et al., 2014) as shown in figure 2.6.

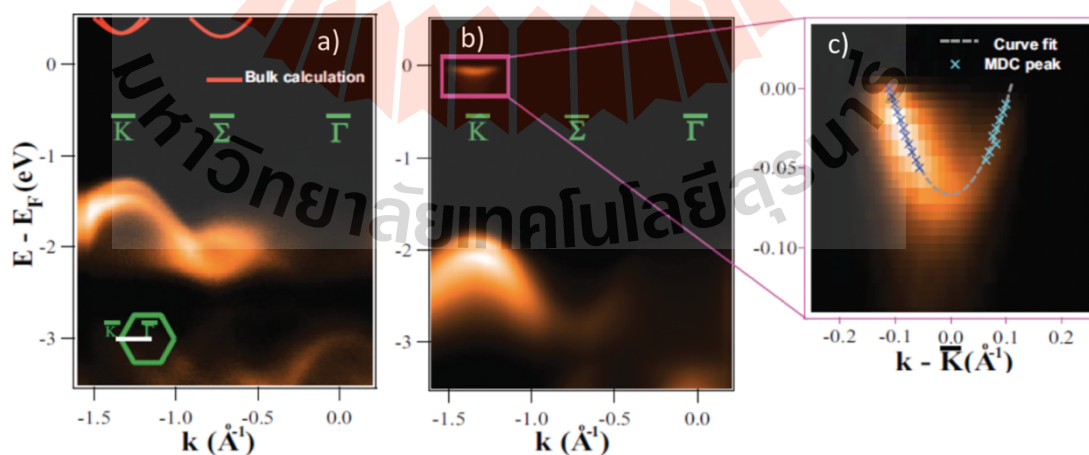


Figure 2.6 a), b) Valence band measured along the $\bar{\Gamma}$ - \bar{K} direction for bulk and monolayer MoS₂ and c) conduction band of monolayer MoS₂ (Eknapakul et al., 2014).

In addition, other properties change as the MoS₂ changes from bulk to monolayer. Kim and his co-worker studied the work function of MoS₂. They found that the work function of 2-to-12 layers of MoS₂ decreased when the layers were decreased. (Kim et al., 2015). Mak and his team trace the effect of quantum confinement on the MoS₂'s electronic structure by using absorption, photoluminescence, and photoconductivity spectroscopy. They found that with decreasing thickness, the indirect band gap, which lies below the direct gap in the bulk material, shifts upwards in energy by more than 0.6 eV. This leads to a crossover to a direct-gap material in the limit of the single monolayer. Unlike the bulk material, the MoS₂ monolayer emits light strongly. The freestanding monolayer exhibits an increase in luminescence quantum efficiency by more than a factor of 10⁴ compared with the bulk material (Mak et al., 2010).

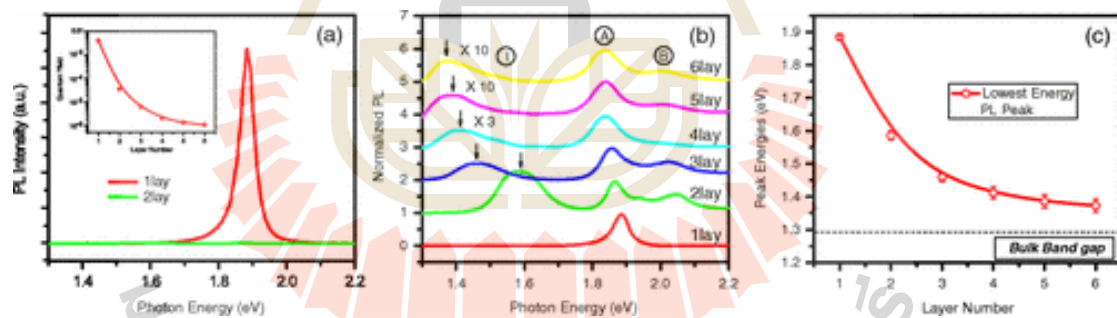


Figure 2.7 a) PL spectra for mono and bilayer MoS₂ samples in the photon energy range from 1.3 to 2.2 eV. Inset: PL QY of thin layers for N = 1 – 6. b) Normalized PL spectra by the intensity of peak A of thin layers of MoS₂ for N = 1 – 6. c) Bandgap of thin layers of MoS₂. The dashed line represents the (indirect) band-gap energy of bulk MoS₂ (Mak et al., 2010).

Graphene is a 2-dimensional material made up of an atomically thin layer of carbon atoms arranged in a honeycomb lattice. The interesting property of graphene, which is important to optoelectronic devices, is carrier multiplication. That means a single photon generates charge carriers more than one by the Auger process (Winzer et al., 2010). Therefore, graphene can generate multiple charge carriers from the absorption of a single photon, as shown in figure 2.8. This can improve the light conversion efficiency of solar cells. Torben and his co-workers used microscopic calculations for carrier multiplication studies. They found that it is estimated that graphene can generate multiple carriers ($CM = 4.3$) when it was induced by the optical excitation (Torben et al., 2010). Plötzing and his team have been reported on the first direct experimental observation of carrier multiplication in graphene reaching a multiplication factor of up to 2 and persisting on a picoseconds time scale (Plotzing et al., 2014).

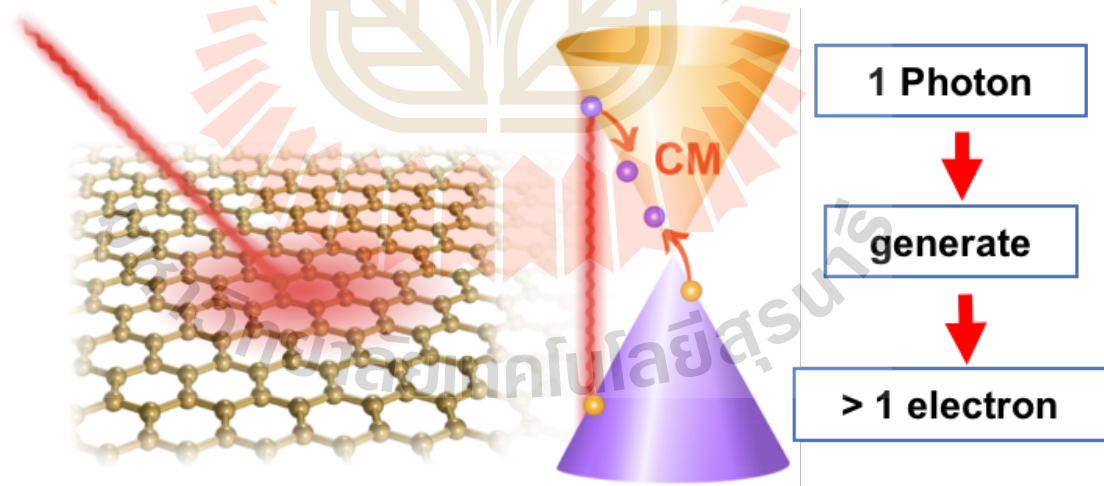


Figure 2.8 Carrier multiplication (CM) process (Torben et al., 2010).

In a photovoltaic device, carrier multiplication enhances charge carrier density, leading to high efficiency of the device. Furthermore, graphene has significantly increased the

photocurrent of photodetectors, resulting in high resolution devices. Normally, graphene is used in combination with other materials, such as graphene/semiconductor heterojunction for photodetectors. Shimatani and co-workers developed a graphene/indium antimonide (InSb) heterojunction photodetector for high-resolution mid-IR image sensors. They found that the carrier density modulation effect of graphene was amplified due to the carrier multiplication effect (Shimatani et al., 2020). Fukushima and his team also studied graphene-based field effect transistors that were fabricated on indium antimonide (InSb) substrates. They found that the InSb generated photo-carriers in response to incident IR light modulated the graphene channel gate voltage and induced a large photocurrent (Fukushima et al., 2018). Additionally to the previous, graphene exhibits exceptional capabilities for terahertz (THz) optoelectronics via the plasmonic effect (Li et al., 2020). Although graphene is a relatively new material system for THz optoelectronics, it has received much interest because of several of unique features (Low and Phaedon, 2014; Tassin, Koschny and Soukoulis, 2013). Therefore, graphene is a potential candidate for optoelectronic devices. Unfortunately, optoelectronic applications need a semi-conductor material, but graphene is a gapless material because the valence band and conduction band of graphene cross at the Dirac point in the Brillouin zone in the reciprocal space. Thus, the gap opening of graphene is essential to optoelectronic applications. Moreover, the energy gap should be intrinsic property of graphene. However, the bandgap of graphene can be opened by applying strain (Ni et al., 2008 and Cocco et al., 2010) electric field (Castro et al., 2007), but these effects are temporary bandgap, the bandgap closes when stop applying strain and electric field. There are many ways to create intrinsic gap in graphene such as substrate inducing (Zhou et al., 2007). In addition, the bandgap of graphene can be generated by

quantum confinement effect. By this effect, the bandgap of graphene depends on size in nano-scale of graphene such as graphene quantum dots (GQDs).

2.5.1 Electric field

Because the Fermi level of pure graphene correlates with its Dirac point, it may be deliberately controlled to constantly move up and down by doping electrons or holes, respectively. One efficient approach for doping electrons and holes is to apply a gate voltage on graphene, as seen in figure 2.9 a. When the Fermi level gets close to the Dirac point, graphene's conductivity drops as the charge carrier density drops. Additionally, the carrier density of graphene may be quantified quantitatively by Hall measurements, allowing for easy calculation of the mobility. The evolutions of n_s and μ with graphene's gate voltage are shown in Figure 2.9 b. As can be observed, charge carrier density grows linearly with gate voltage absolute value (notice that positive and negative gate voltages correspond to electron and hole doping, respectively), and mobility rises rapidly as the shifted Fermi level approaches the Dirac point (Zhan et al., 2012). Graphene's electrical properties also depend on its stacking geometry. The AB sequence stacks the most potentially favorable bilayer graphene (BLG). Unlike single-layer graphene (SLG), which exhibits just one linear band in the low-energy regime, BLG exhibits two groups of parabolic bands owing to the interlayer coupling effect. Thus, by modulating the electronic coupling between layers, the electronic band structure of these parabolic bands may be modified.

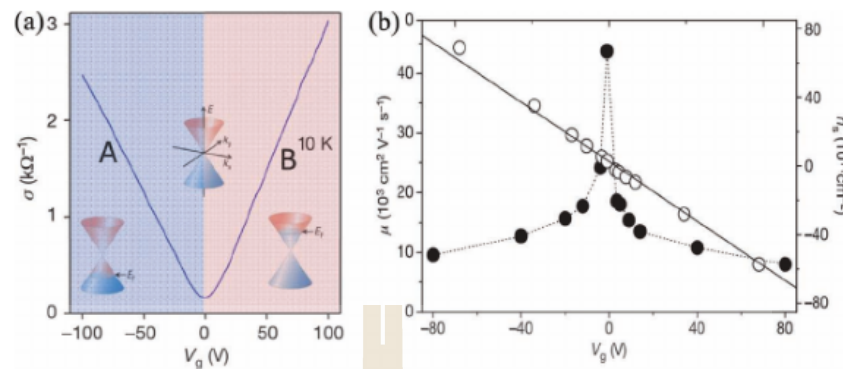


Figure 2.9 a) The conductivity of graphene as a function of gate voltage measured at 10 K. The blue (A) and red (B) regions represent the hole- and electron-doped graphene. The insets show the electronic spectra of positively (left), neutrally (middle), and negatively (right) doped graphene at around the Dirac point. b) Charge carrier density n_s (open circles) and mobility μ (solid circles) of graphene as a function of gate voltage (Zhan et al., 2012).

Graphene electrons travel at near-light speed. Graphene's promise for electronics and photonics requires a bandgap. Ohta and colleagues report on the angle-resolved photoemission characterization of bilayer graphene thin films on insulating silicon carbide. The potassium doping increased the carrier concentration in each layer, allowing regulation of the valence-conduction band gap. Figure 2.10 illustrates the evolution of gap closing and reopening when the doping level is varied by potassium adsorption (Ohta et al., 2006). Zhang and colleagues engineered a bandgap in BLG that is perfectly controllable between 0 and 250 meV by tunable electric field. The electric field used in BLG and the bandgap opening are shown schematically in figure 2.11 a. As seen in figure 2.11 b, experimental results (red squares) are contrasted to theoretical predictions based on self-consistent tight-binding (Zhang et al., 2009).

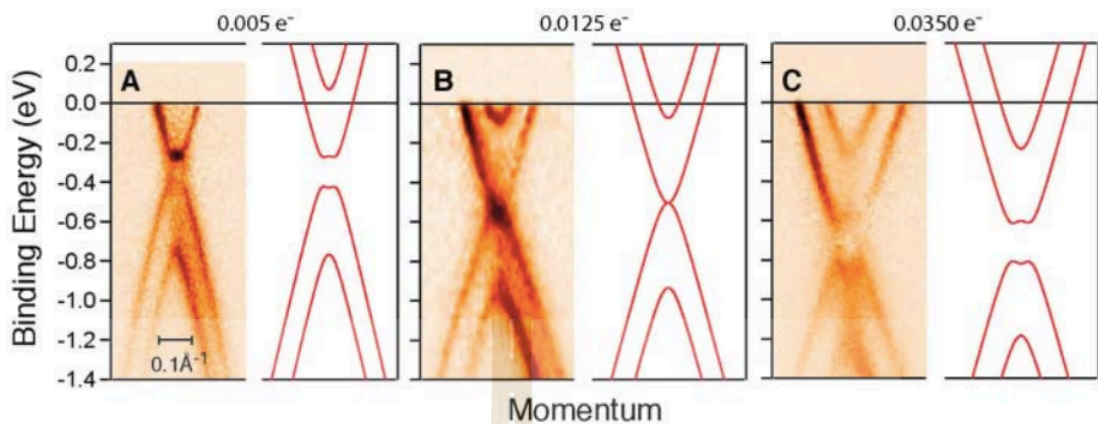


Figure 2.10 Evolution of gap closing and reopening by changing the doping level by potassium adsorption. Experimental and theoretical bands (solid lines) (A) for an as-prepared graphene bilayer and (B and C) with progressive adsorption of potassium are shown. The number of doping electrons per unit cell, estimated from the relative size of the Fermi surface, is indicated at the top of each panel (Ohta et al., 2006).

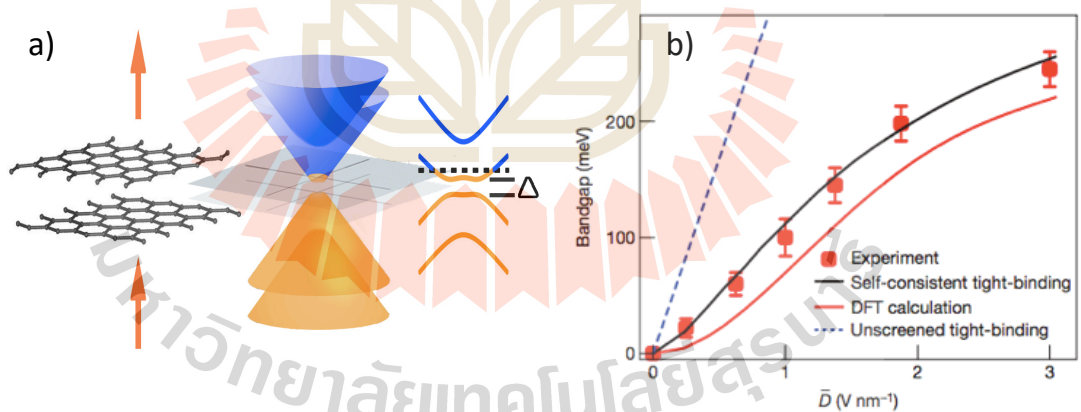


Figure 2.11 a) Schematic of electric field that was applied in BLG and bandgap opening. b) Experimental results (red squares) are contrasted to theoretical predictions derived from self-consistent tight-binding calculations (black trace), ab initio density functional calculations (red trace), and unscreened tight-binding calculations (red trace) (blue dashed trace) (Zhang et al., 2009).

2.5.2 Strain

Because graphene is a two-dimensional material, both symmetrical strains that maintain hexagonal symmetry and asymmetrical strains that degrade hexagonal symmetry are generally considered. Strain is the material's deformation or displacement as a consequence of an applied force. The strain relationship is as follows

$$\varepsilon = \frac{L-L_0}{L_0} \quad (2.7)$$

where ε is strain, L is length after applied force, and L_0 is original length.

Tensile and compression strains are normally applied to the atomic structure of materials. Strain would distort the Brillouin zone correspondingly as the unit cell changed in real space. The symmetrical tensile strain crushes the unit cell of graphene uniformly, bringing the electronic bands closer to the Fermi level and modifying the band dispersion in the momentum space. The symmetrical compressive strain effect follows the inverse trend of the tensile strain effect. Tensile strains of up to 0.8 percent were applied to graphene deposited on a flexible substrate, resulting in significant red shifts in the Raman spectra of the 2D and G bands, as illustrated in figure 2.12 a .Raman spectra changes due to the elongation of carbon-carbon bonds. Furthermore, first-principle simulations predict that graphene would have a bandgap opening when subjected to uniaxial tensile strain, as shown in figure 2.12 c (Ni et al., 2008).

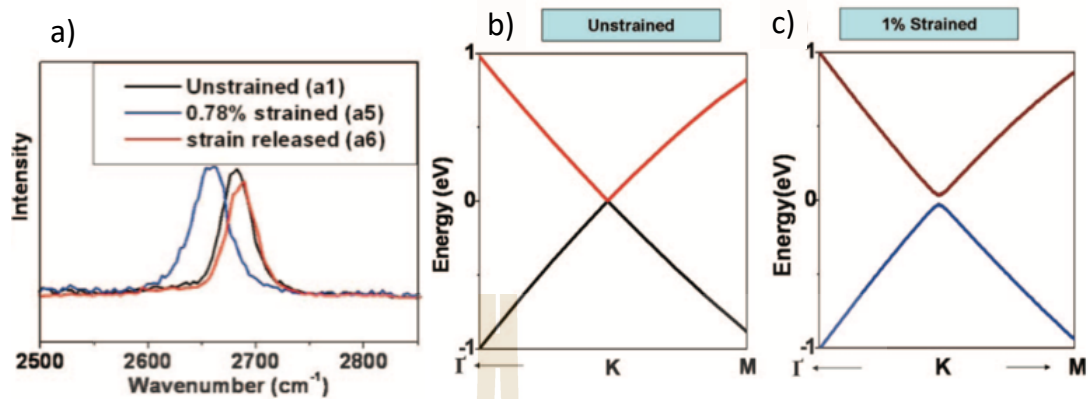


Figure 2.12 a) The Raman spectra that are taken from the 2D band SLG. b) and c) Calculated band structure of unstrained and 1% tensile strained graphene (Ni et al., 2008).

Because the electronic band structure of layered graphene may be modified by the coupling between layers, strain also effects the band dispersion of layered graphene different single layers because of the coupling between layers. When tensile strain is applied in a zigzag direction, the bandgap of a single layer is greater than that of bilayers at the same percent strain, as seen in figure 2.13 (Wong, Wu and Lin, 2012).

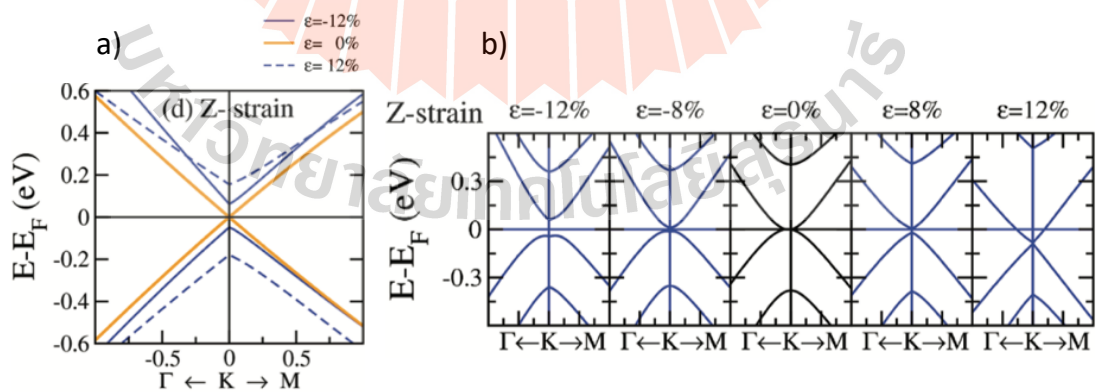


Figure 2.13 a) The band structure of single layer graphene at the K point under zigzag strain. b) The band structure of bilayer graphene at the K point when applied to a zigzag strain (Wong, 2012).

The following techniques for inducing strain have previously been shown to be practical and are now being used with layered materials: bending flexible substrates, elongating an elastic substrate, piezoelectric stretching, substrate thermal expansion, and controlled wrinkling as illustrated in figure 2.14 (Roldán et al., 2015).

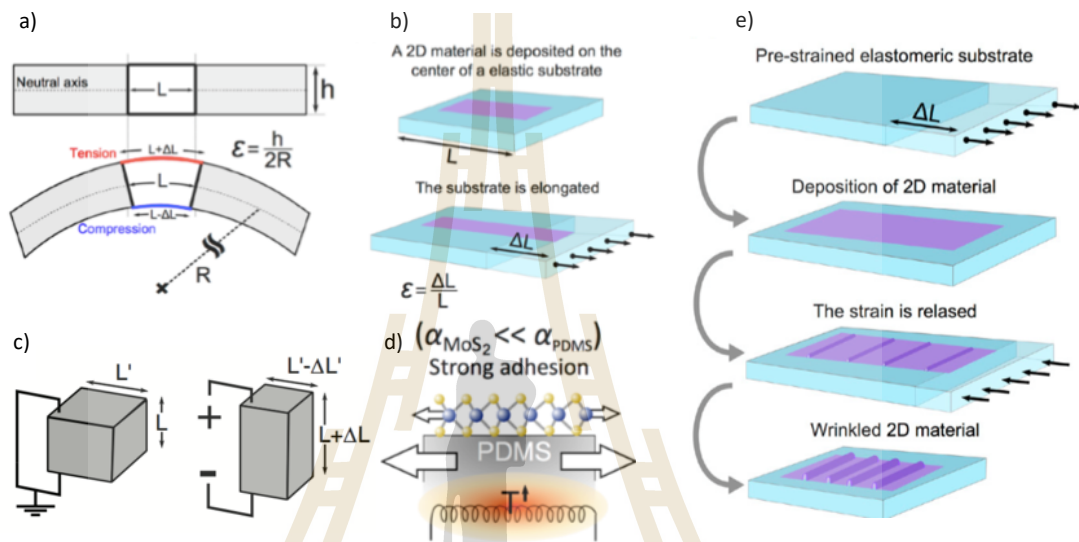


Figure 2.14 a) Scheme of the cross section of the flexible substrate before and after bending it. b) Scheme of the approach to apply uniaxial tensile strain by elongating an elastic substrate. c) Schematic diagram of the mechanical deformation of a piezoelectric material when an electric field is applied. d) Schematic diagram of the process to strain atomically thin materials by using substrates with strong adhesion and very large thermal expansion coefficient. e) Schematic diagram of the fabrication process of wrinkled nanolayers (Roldán et al., 2015).

2.5.3 Quantum confinement effect

In general, a bulk material's free electrons can travel freely in all directions. When a bulk material is decreased in one direction (two-dimensional materials) or in all directions (quantum dots), the electrons are also limited in their

movement. Electrons are described by quantum confinement effects in terms of energy levels, potential wells, valence bands, conduction bands, and electron energy band gaps. When the particle's size is too small to be equivalent to the electron's wavelength, the quantum confinement effect is observed. Essentially, the confinement of an electron and a hole in nanostructures affects their electrical and optical characteristics significantly. Size and shape have an effect on the electrical and optical properties of materials. Well-known technological breakthroughs, such as quantum dots, were obtained from size manipulation and theoretical confirmation of the quantum confinement effect. Quantum confinement is explained using the particle in a box paradigm, in which an electron is free to travel in a limited area. By reducing the volume or dimensions of the accessible space, the energy of the states is increased. The relationship between energy level and dimension spacing is seen in the following equation:

$$E_{n_x n_y n_z} = \frac{\hbar^2 \pi^2}{2m} \left[\left(\frac{n_x}{L_x} \right)^2 + \left(\frac{n_y}{L_y} \right)^2 + \left(\frac{n_z}{L_z} \right)^2 \right] \quad (2.8)$$

Where $E_{n_x n_y n_z}$ is energy level and L_x , L_y and L_z are dimension spacing of x, y and z.

The difference in electron energy level and bandgap between a nanomaterial and its bulk state is seen in figure 2.15.

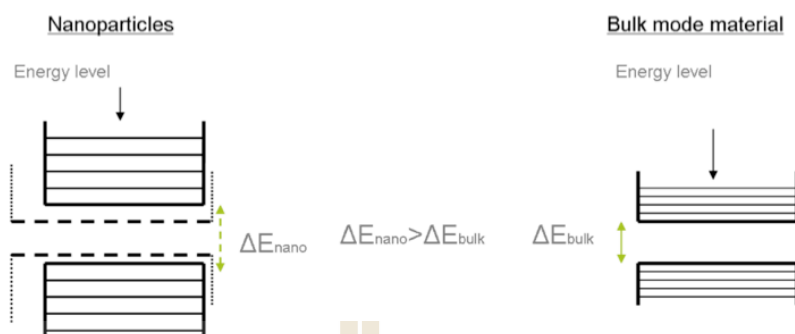


Figure 2.15 Bandgap difference of nanoparticle and bulk material.

By using density-functional theory (DFT) and time-dependent DFT calculations, Mahasin Alam Sk, et al. have found that the optical property of a GQD can be sensitively tuned by its size. Therefore, increasing the size resulted in an increasing in the emitted wavelength as shown in figure 2.16 a (Sk et al., 2014). Moreover, the study of Goki Eda using the DFT calculation found that bandgap of graphene dots (benzene ring) decrease when sizes of the dots increase as shown in figure 2.16 b (Eda et al., 2010).

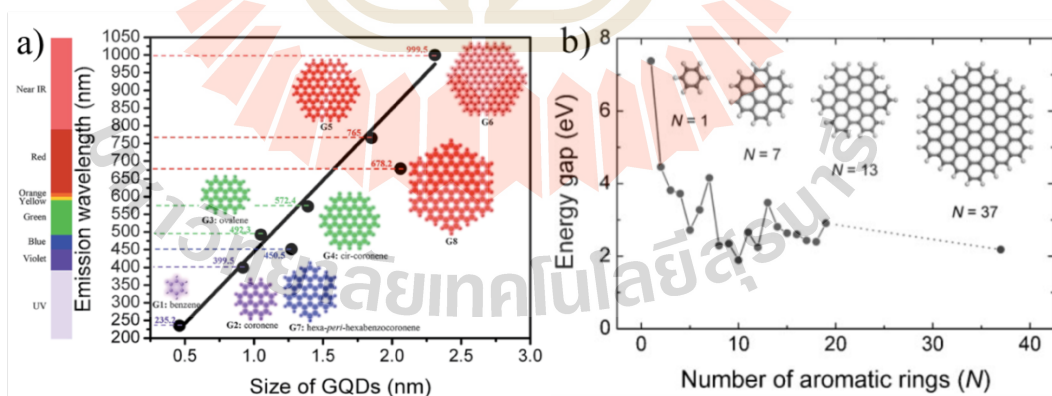


Figure 2.16 a) Calculated emission wavelength (nm) using TDDFT method in a vacuum as a function of the diameter of GQDs (Sk et al., 2014). b) The bandgap of graphene dots (benzene ring) calculated based on DFT as a function of the number of fused aromatic rings (N) (Eda et al., 2010).

The bandgap of graphene quantum dots has received the most attention due to their photoluminescence (PL) property. Peng and co-workers synthesized GQDs with different sizes of 1-4 nm, 4-8 nm, and 7-11 nm by varying the reaction temperatures. They found that GQDs with different sizes of 1-4 nm, 4-8 nm, and 7-11 nm emitted different PL blue, green, and yellow, respectively, as shown in figure 2.17 (Peng et al., 2012). This result revealed the different types of PL that depend on the size of GQD. Moreover, Kim also reported that the visible photoluminescence (PL) of GQD varied sizes from 5–17 nm, which is consistent with the quantum confinement effect (QCE) (Kim et al., 2012).

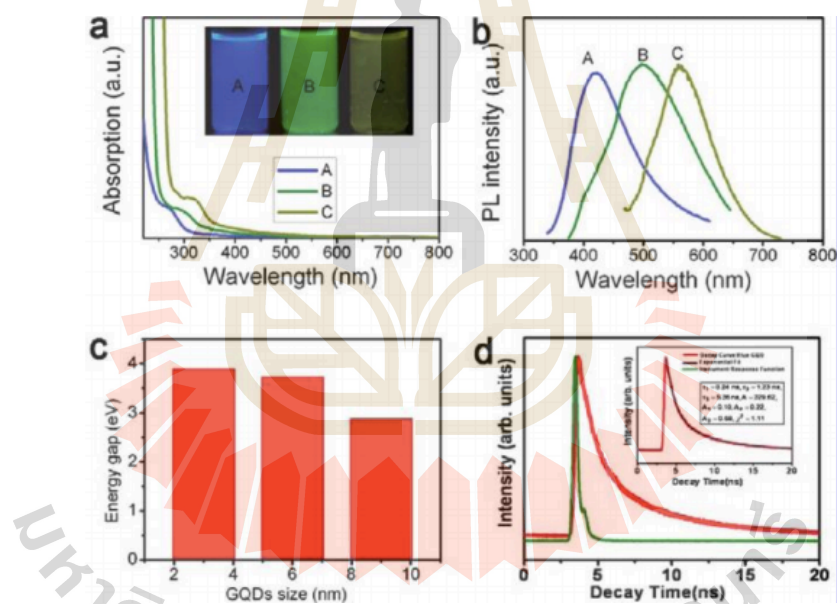


Figure 2.17 Optical properties of the GQDs. (a) UV–vis spectra of GQDs 1-4 nm (A), 4-8 nm (B) and 7-11 nm (C). Inset of panel a is a photograph of the corresponding GQDs under UV light with 365 nm excitation. (b) PL spectra of GQDs with different emission color excited. (c) Relationship between the energy gap and the size of GQDs. (d) TRPL decay profile of blue GQDs recorded at room temperature. The inset shows the lifetime data and the parameter generated by the exponential fitting (Peng et al., 2012).

However, the bandgap of GQDs is not dependent on only the QCE because GQDs consist of graphene nanostructure and surface chemical groups that bond with the graphene nanostructure. These chemical groups may contribute to UV-visible absorption. (Wang et al., 2014 and Wang et al., 2013). So, the bandgap of perfect nanocrystalline graphene is interesting to study.

2.5.4 Edge

Perfect graphene crystalline is a candidate for a variety of applications and also requires band gap opening procedures. Cutting graphene to the nanoscale is one of the few methods for opening a band gap while retaining graphene's excellent mobility. The graphene edge is formed by shrinking the graphene to a smaller size. Localized electron distribution is determined by edge configurations, and so the crystallographic orientation of graphene is critical for determining its electronic characteristics in localized states. As seen in Figure 2.18, zigzag and armchair edges are the two primary forms of graphene edges along crystallographic axes (Zhang, Xin, and Ding, 2013).

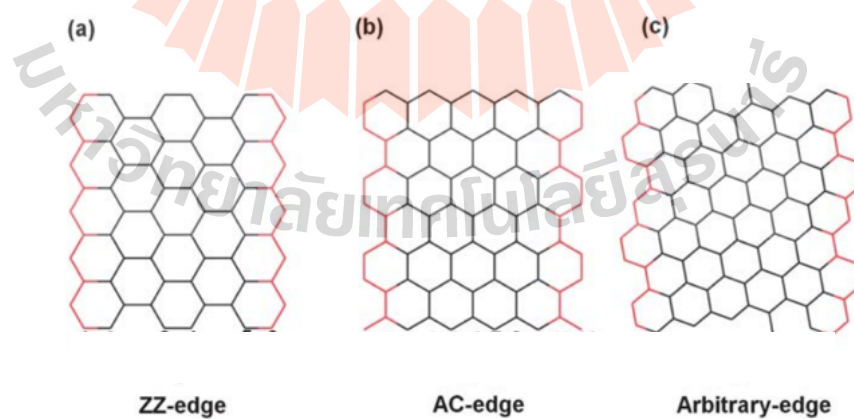


Figure 2.18 The red line are a) zigzag edge of graphene nano ribbon (GNR), b) armchair edge of graphene nano ribbon and c) arbitrary edge of graphene nano ribbon (Zhang et al., 2013).

The orientations of graphene flakes' edges might well be identified using a high-resolution STM capable of producing atomic-resolution pictures of the graphene crystal lattice, allowing for unequivocal identification of armchair or zigzag edges. The electronic structure of the nanoscale graphite material is significantly influenced by its edge. Although the energy gap of graphene nanoribbons (GNRs) with comparable widths differs due to their opposed edges (zigzag and armchair), this impact is negligible when compared to the quantum confinement effect (Ritter et al., 2009).

2.5.5 Disorders in graphene structure

During the production process, disorder may also be induced in the graphene crystal structure. With a limited dimension, graphene's changed massively from unevenly formed edges, stacking disorder between two layers, and atomic defects inside the layer. Raman spectroscopy is useful for identifying structural defects in graphite-base materials. The oscillation mode of Raman spectroscopy that describes the disorder structure of graphite-base materials is the D-band, which arises at around 1350 cm^{-1} . By adding disorder to the graphene structure, the electronic homogeneity of the graphene would be broken. These disorders are capable of modifying the bond lengths of interatomic bonds and re-hybridizing the σ and π orbitals. Additionally, any imperfections may scatter electron waves and alter electron paths. The defect created by the borders between the intrinsic and N-doped areas can create a zero-energy gap in graphene of about 130 meV (Bai et al., 2014).

2.6 Nano patterning for devices fabrication

As I mentioned above, the nanostructure of layered materials is interesting because of the electronic structure engineering of these materials. Moreover, nano patterns of materials also affect the properties of devices. Normally, nano patterns are prepared by the lithography technique. As shown in Figure 2.19, Neu and his team fabricated single-crystalline diamond nanopillars on a (111)-oriented chemical vapor deposited diamond substrate as shown in Figure 2.20. They characterized single native NV centers in these nanopillars and found the highest reported saturated fluorescence count rates in single crystalline diamond in excess of 10^6 counts per second on this device. They show that their nano-fabrication procedure conserves the preferential alignment as well as the spin coherence of the NVs in our structures. (Neu et al., 2014).

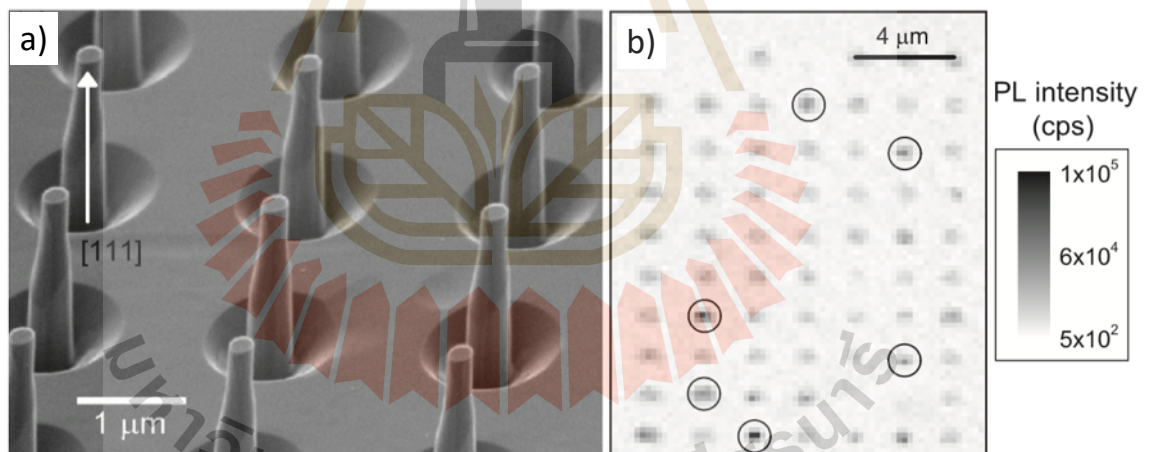


Figure 2.19 a) Scanning electron microscopy image of diamond nanopillars fabricated on a (111)-oriented single-crystalline diamond sample. b) Confocal fluorescence image of an array of diamond nanopillars (Neu et al., 2014).

Refractive index property were investigated in nano pattern photonic devices. Pina-Hernandez and co-worker fabricated two-dimensional (2-D) photonic crystals as well

as 1D and 2D photonic nanocavities. They observed enhanced photoluminescence from the 2D photonic crystal and the 1D nanocavities (Pina-Hernandez et al., 2017). Neder, Luxembourg, and Polman fabricated silicon heterojunction solar cells integrated with arrays of light scattering dielectric nanoscatterers by using substrate-conformal soft-imprint lithography. By using green spectrum as incident light, they found that this device exhibited high performance because of resonant spectrum nanoscatterers (Neder, Luxembourg, and Polman, 2017).

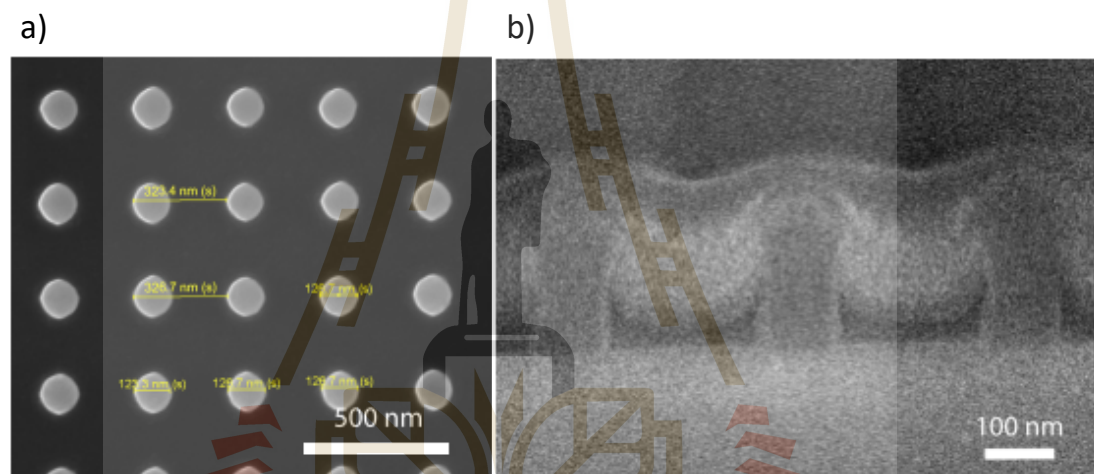


Figure 2.20 a) Top-view SEM image of a square array of silicon nanoscatterers on a sapphire cover slide, made by SCIL. b) SEM image of a cross section of the silicon nanoscatterers on sapphire made using focused ion beam milling (Neder, Luxembourg, and Polman, 2017).

Researchers have been attracted to graphene's pattern by the lithography technique. Ju and his team investigate plasmon excitations in arrays of engineered graphene micro-ribbons as shown in figure 2.21. They reveal that by varying the micro-ribbon width and in situ electrostatic doping, graphene plasmon resonances can be adjusted over a broad terahertz frequency range (Ju et al., 2011).

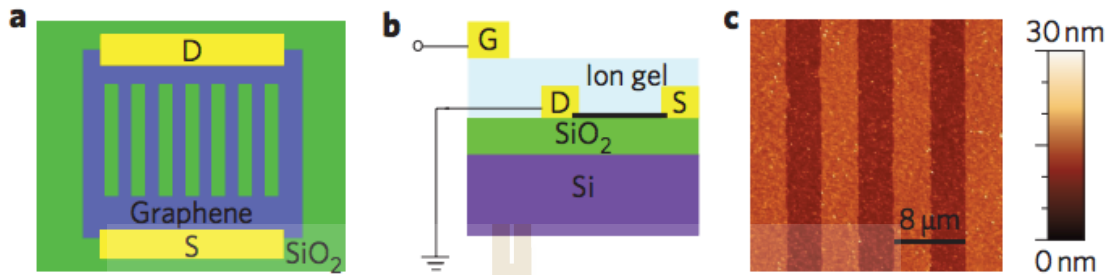


Figure 2.21 a) A typical graphene micro-ribbon arrangement from the top. b) A typical device with a graphene micro ribbon array on a Si/SiO₂ substrate from the side. c) AFM image of a graphene micro-ribbon array sample (Ju et al., 2011).

Furthermore, graphene can be improved by a periodic array of metallic nanoparticles. Tantiwanichapan and his team investigate the excitation of THz plasmon polaritons in large-area graphene samples on standard oxidized silicon substrates via diffractive coupling from an overlying periodic array of metallic nanoparticles. They found that an array of Au nano particles enhanced surface-plasmon resonances at THz frequencies via array period decreased (Tantiwanichapan et al., 2017).

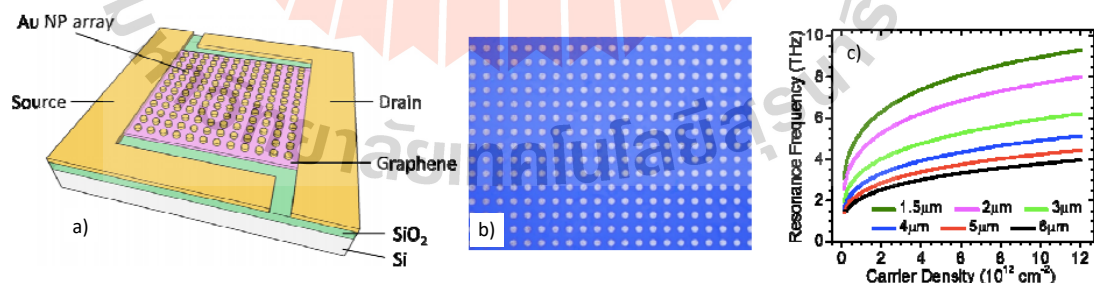


Figure 2.22 a) The investigated device geometry is represented schematically. b) Optical microscope taken from the top of a device with an array period(Λ) = 6 μm . c) Calculated resonance frequency of grating-coupled GPPs, plotted as a function of carrier density N for different values of Λ (Tantiwanichapan et al., 2017).

Although lithography is a famous method for nano pattern preparation, but it can also become contaminated with solvents through this process. The contaminated of layered materials are directly effect on their properties. Therefore, nanoscale layered materials require a technique that non-contact with solvents for high purity nanoscale layered materials. By the way, electronic and optoelectronic applications require single crystalline material, because it absence of imperfections such as grain boundaries, inhomogeneous strain, and dislocations (Zhang, Dong and Hu, 2018; Murali et al., 2019). This absence gives single crystals unique characteristics, especially mechanical, optical, and electrical, which depend on the crystallographic structure. Therefore, the way to open a gap in single crystal graphene that is suitable for optoelectronic devices was investigated. The reason for this leads us to the selection of methods for preparing nanoscale layered materials for use in the study of electronic structure.



CHAPTER III

MATERIALS AND METHODOLOGY

In this chapter, we will discuss layered materials, the process of preparing nanopatterns and measuring techniques including angle resolved photoemission spectroscopy (ARPES), Raman spectroscopy and how to calculate bandgap as a tensile strain induced by using density functional theory (DFT).

3.1 Layered material

3.1.1 Graphene

Graphene is one kind of carbon structure which is made up of a single layer of atoms arranged in a two-dimensional honeycomb lattice. One of atom in graphene is connected to three closest by a σ bond as shown in figure 3.1 a. Three of valence electrons of each atom in the graphene occupy three sp^2 hybrid orbitals, which combine s , p_x and p_y orbitals. The remaining electron of valence is perpendicular to the plane and occupies a p_z orbital. These orbits are hybridized into two semi-filled strips of free-moving electrons, π and π^* , which represent the majority of the remarkable electronic features of graphene (Cooper et al., 2012). Electronic structure of graphene exhibit a semimetal feature that conduction (p_z orbital) and valence bands (p_z orbital) overlap at the Dirac points, which are six locations in Brillouin zone, divided into two non-equivalent sets of three points (labeled K and K' in the Brillouin zone). The two bands touch at the zone corners where there is a zero density of states but no band gap as exhibited in figure 3.1 b.

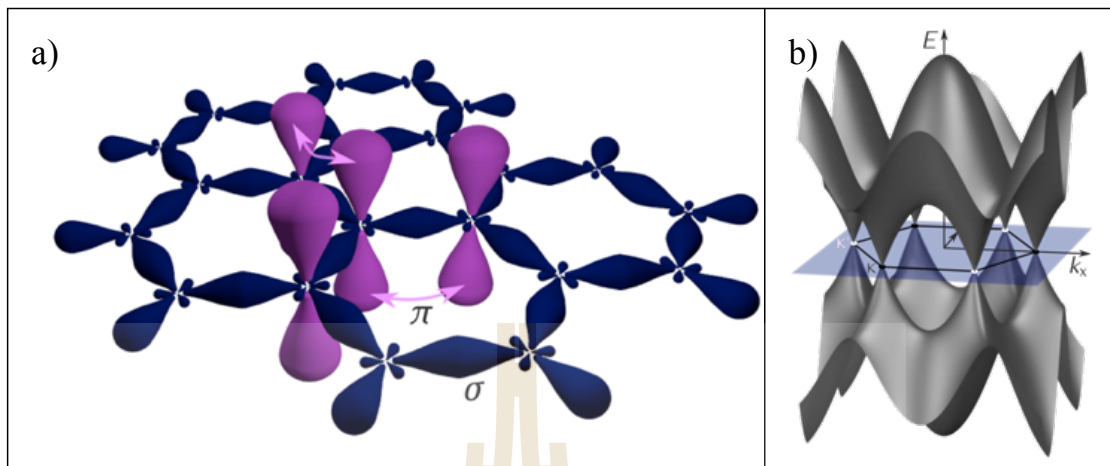


Figure 3.1 a) Sigma and pi bonds in graphene. Sigma bonds result from an overlap of sp² hybrid orbitals, whereas pi bonds emerge from tunneling between the protruding p_z orbitals. b) Electronic structure of graphene. Valence and conduction bands meet at the six vertices of the hexagonal Brillouin zone and form linearly dispersing Dirac cones (Cooper et al. 2012).

In low energies, the electrons can be characterized by a formally equivalent equation of the massless Dirac equation and even ignore the intrinsic spin. As a result, electrons and holes are referred to as Dirac fermions. This pseudo-relativistic description is confined to the chiral limit, i.e., to vanishing massless M_0 , which leads to additional features:

$$v_F \sigma \cdot \nabla \psi(r) = E \psi(r) \quad (3.1)$$

Here v_F is the Fermi velocity in graphene, which replaces the velocity of light in the Dirac theory; σ is the vector of the Pauli matrices; $\psi(r)$ is the two-component wave function of the electrons and E is their energy. The mass of the charge carrier in graphene is of interest because it enables the development of novel properties. If the mass of graphene can be controlled, electrons can be limited to massless regions by

enclosing them in massive regions, enabling the patterning of quantum dots, wires, and other mesoscopic structures. Additionally, it generates one-dimensional conductors parallel to the boundary. These wires would be impervious to backscatter and capable of carrying current without dissipating it. (Fuhrer, 2013)

Carrier multiplication, a mechanism that has been extensively researched in the aspect of increasing the efficiency of solar energy conversion, brings attention to graphene in optoelectronic applications. Multiple charge carriers are created as a result of a single photon's absorption by Auger processes. Auger processes are classified into two types: Auger recombination (AR) and impact ionization (II), as shown in figure 3.2. (Winzer et al., 2010)

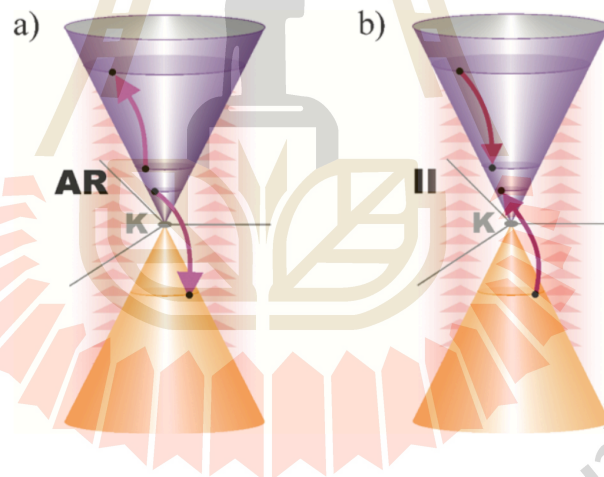


Figure 3.2 a) Auger recombination (AR) b) Inverse Auger recombination or impact ionization (II) (Winzer et al., 2010).

Figure 3.2 exhibits the linear energy dispersion of graphene around the K point. After an optical excitation (depicted by red arrows), the hot carriers relax toward equilibrium via Coulomb-induced scattering processes. As shown in figure 3.2 a, AR is a process in which one electron is scattered from the conduction band into the valence band while

transferring energy to another electron excited to a more energetic state inside the conduction band. Inverse Auger recombination is the inverse process of II. When an electron relaxes to a lower energy state, it excites a valence band electron into the conduction band, as shown in figure 3.2 b. As a result of II, the carrier density increases (carrier multiplication).

Graphene is attractive for optoelectronic applications due to its plasmonic properties. Plasmonics is typically based on so-called surface plasmon polaritons (SPPs), which are coherent electron oscillations traveling along the interface between a dielectric (e.g. glass, air) and a metal (e.g. silver, gold). Graphene has also demonstrated surface plasmon phenomena comparable to those of metallic thin films. The plasmonic characteristics of hybrid structures can be modified to improve optoelectronic device performance by engineering metallic substrates or nanoparticles (e.g., gold, silver, and copper) with graphene. Additionally, graphene exhibits plasmonics on its own. At low energies where the wavelengths surpass the damping length, graphene plasmons can also be isolated from their environment and generate real Dirac plasmons. The intrinsic graphene plasmons are strikingly different from noble metal plasmons in that they can be tuned by gated or doped graphene. Graphene plasmonic resonances may play a critical role in the development of robust and inexpensive terahertz photodetectors with significant security applications.

3.1.2 Highly oriented pyrolytic graphite

Highly oriented pyrolytic graphite (HOPG), ultra-pure graphite, has a high degree of preferred crystallographic orientation of the c-axes perpendicular to the surface of the substrate. HOPG was prepared by the deposition of a layer of graphene on a substrate at a high temperature in a vacuum, such as graphitization heat treatment

of pyrolytic carbon or by chemical vapor deposition at high temperatures. Although HOPG is the bulk of graphene, its conduction and valence bands still overlap at high symmetry points in the Brillouin zone and reveal a Dirac fermion as shown in graphene (Orlita et al., 2008; Luk'yanchuk and Kopelevich, 2006). The Fermi surface of graphene or graphite single layer shows small dots of high intensity located at the six corners of the hexagonal Brillouin zone. For the HOPG, the Fermi energy intensity map shows a perfectly circular pattern in contrast to what is expected for single crystalline graphite. This is attributed to the angular spread of the dots into a circle due to the azimuthal disorder of graphite, as shown in figure 3.3. Although HOPG's Fermi surfaces are significantly different from graphene, Zhou, et. al, observed an angular average of the calculated dispersions to prove the difference in the band dispersion at each azimuthal angle. They discovered that the band dispersion of azimuthal angles has no discernible angular dependence, indicating that this material has an azimuthally invariant electronic structure (Zhou et al., 2005).

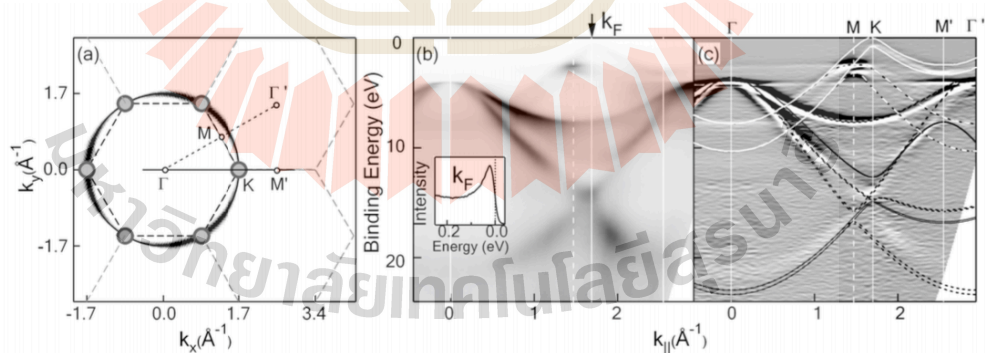


Figure 3.3 a) The hexagonal Brillouin zone dashed lines and Fermi surface shaded circles expected for single crystalline graphite are drawn schematically. b) Intensity map vs binding energy and in-plane momentum along the solid line in a taken at 60 eV photon energy. The inset shows energy distribution curve EDC at k_F taken at 25 eV. c) Second derivative of raw data in b with respect to energy (Zhou et al., 2005).

3.1.3 Transition metal dichalcogenides

Transition metal dichalcogenides (TMDs) are the most investigated layered materials at the moment. TMDs are indicated by the chemical formula MX_2 , where M represents a transition metal (Mo, W) and X represents a chalcogen (S, Se). Each layer of TMDs is around 6 – 7 Å thick, comparable to graphene. Each in-layer of these materials is held together by strong ionic bonds, but surrounding planes are held together by a weak van der Waals (vdW) force that is many orders of magnitude less than the in-plane contact. Atomic structure of TMD demonstrate in figure 3.4.

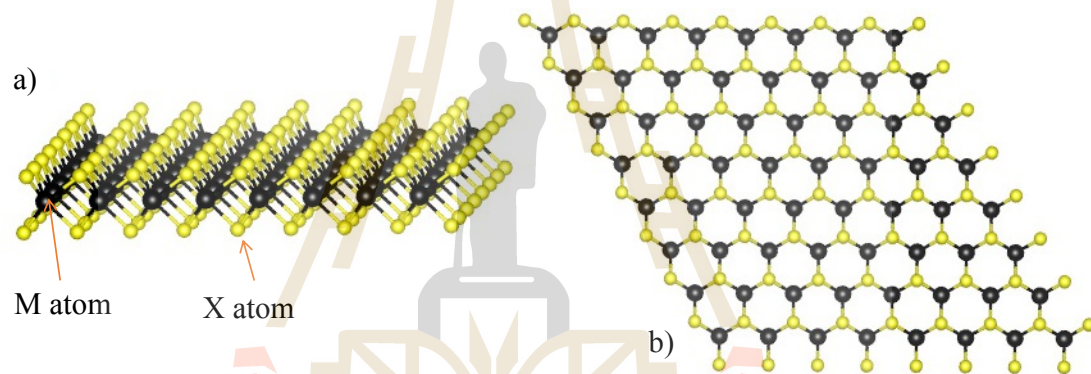


Figure 3.4 a) Side-view of atomic structure of transition metal dichalcogenides (TMD) where M represents a transition metal and X represents a chalcogen. b) Top-view of atomic structure of transition metal dichalcogenides (TMD).

Layered TMDs are formed by stacking hexagonal packed planes containing three or six chalcogens around a central metal atom in a trigonal prismatic configuration. The low vdW force between each layer of TMDs results in an unique cleavage property perpendicular to the out-of-plane axis. There are around eighty different stacked TMD compounds with properties ranging from insulating to superconducting. Mo- and W-based TMDs, in particular, are semiconductors with a tunable band gap of 1.5–2.1 eV

(Frey et al., 1998; Kuc et al., 2011), and are the most extensively investigated materials apart from graphene. Two-dimensional semiconductors constructed from ultrathin TMDs have promising applications for novel electronic device applications; for example, a high emission in the visible frequency region is advantageous in optoelectronics (Wilson and Yoffe, 1969).

3.2 Nano-pattern preparation

3.2.1 Focused ion beam

The technology of focused ion beam (FIB) was primarily developed in the late 1970s and early 1980s. Modern FIB systems are increasingly being used in semiconductor research and manufacturing settings, as well as in failure analysis and chip design centers. A FIB setup is a basic scientific device for a scanning electron microscope (SEM). While the SEM uses a focused beam of electrons to view the sample within the chamber, the FIB employs a focused beam of ions. Additionally, FIB can be integrated into a system that includes both electron and ion beam columns, allowing for the investigation of the same feature utilizing either of the beams. FIB really shouldn't be confused with direct write lithography, which utilizes a focused ion beam. A source of the ion beam is liquid metal ion sources (LMIS), especially gallium ion sources. When energetic ions hit the surface of a solid material, they lose energy to the electrons of the solid as well as to its atoms. The most important physical effects of incident ions on the substrate are: sputtering of neutral and ionized substrate atoms, electron emission, displacement of atoms in the solid, and emission of phonons. Chemical interactions include the breaking of chemical bonds, thereby dissociating molecules. When the gallium (Ga^+) initial ion beam interacts with the sample surface, a small

quantity of material is sputtered. The most significant physical effects of incident ions on the substrate are the sputtering of neutral and ionized substrate atoms (which enables substrate milling), electron emission (which enables imaging but may result in sample charging), atom displacement within the solid (induced damage), and phonon emission (heating). FIB can be separated into three processes: i) imaging, ii) site-specific milling, and iii) metal deposition and patterning. Figure 3.5 shows the principles of FIB: a) imaging, b) milling, and c) deposition (Reyntjens and Puers, 2001).

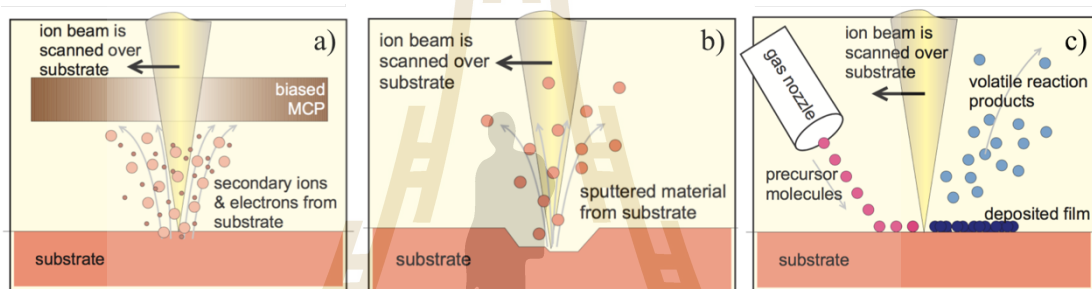


Figure 3.5 Principle of FIB a) imaging, b) milling and c) deposition. (Reyntjens and Puers, 2001).

As seen in figure 3.5 a, FIB imaging involves raster scanning a tightly focused ion beam over a substrate, generating secondary particles (neutral atoms, ions, and electrons) in the sample. The electrons or ions are captured on a biased detector as they exit the sample. As a consequence, physical sputtering of sample material occurs, as schematically represented in figure 3.5 b. When high-energy gallium ions interact with the sample, atoms sputter off the surface. Additionally, gallium atoms will be implanted into the top few nanometers of the surface, resulting in an amorphous surface. As shown in figure 3.5, FIB enables the localized maskless deposition of both metal and insulator materials, as shown in figure 3.5. The main advantages of FIB are the high flexibility in the forms that may be created and the high resolution that can be achieved. The size

of the structures that may be created is limited by the processing time available. The downside of FIB is its poor processing speed. As a result, only very tiny structures (usually in the tens of micrometers) can be produced in an acceptable amount of time. The technology is best suited for post-processing or prototype manufacturing on a small scale.

3.2.2 E-beam lithography

Lithography is a technique for patterning multiple components on a surface, including conductors, semiconductors, and dielectrics. Nanopatterning enables the submicron-sized use of classic lithographic processes. A common patterning procedure involves the formation of several patterned thin films of metals, dielectrics, and semiconductors on a wide range of substrates. This kind of device is manufactured using a process called lithography, which involves the use of radiation-sensitive polymeric compounds called resists to create circuit patterns on the substrates. The sequence of the lithographic process is shown in Figure 3.6.

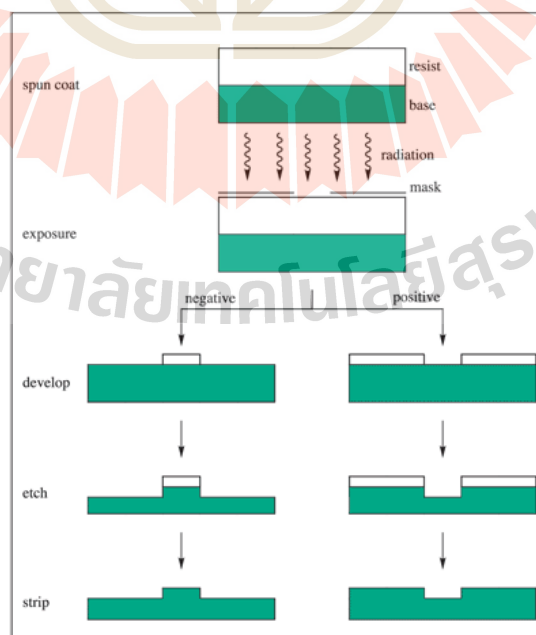


Figure 3.6 Schematic representation of the lithographic process.

Electron beam lithography is the process of irradiating a resist-sensitive surface using an electron beam. The energy absorption in specified regions results in intramolecular processes that determine the polymeric layer's characteristics. Three steps compose this lithography process: irradiation of the sensitive material, resist development, and pattern transfer. It is necessary to keep in mind that these cannot be accomplished in isolation, and that the ultimate resolution is contingent upon the cumulative influence of each individual step in the process. In a direct-write EBL system, the designs are specified directly by scanning the energetic electron beam, and then the sensitive material is transformed physically or chemically as a result of the electron beam's energy deposit. As a result, the shape and characteristics of the electron beam, the energy and intensity of the electrons, the molecular structure and thickness of the resist, the electron–solid interactions, the chemistry of the developer in the resist, the development and irradiation conditions, from the structure design to the beam deflection and control, are all critical for the results.

3.2.3 Nanoscale crystalline preparation

The nanocrystalline was prepared from highly oriented pyrolytic graphite (HOPG) by SpectrumInstrument (HOPG YZA Quality, piece size 7x7 mm., thickness 0.8–1.8 mm.) by focus ion beam (FIB), which used Gallium liquid metal as an ion beam source. The FIB is inside the Field Emission Scanning Electron Microscope (FE-SEM) as shown in figure 3.7. In this work, we prepared the sample by using FE-SEM at the center for scientific and technology equipment at Suranaree University of Technology.



Figure 3.7 Field Emission Scanning Electron Microscope (FE-SEM) at the center for scientific and technology equipment, Suranaree University of Technology.

The samples were sputtered under the FIB probe at 300 kV, 100 pA of the ion beam source and 30 nm of the ion beam size. The ion beam sputtered on the substrate at 300 nm of depth and created an array of nano HOPGs. We used the array pattern shown in figure 3.8 a as a mask for the ion beam. We prepared a nano pattern under 700x magnification of FE-SEM and took 4 masks on the surface of the sample surface as shown in figure 3.8 b. An ion beam will sputter the sample surface following the mask lines. The ion beam operation takes approximately 2 hours for an area of approximately 100 x 100 square micrometers.

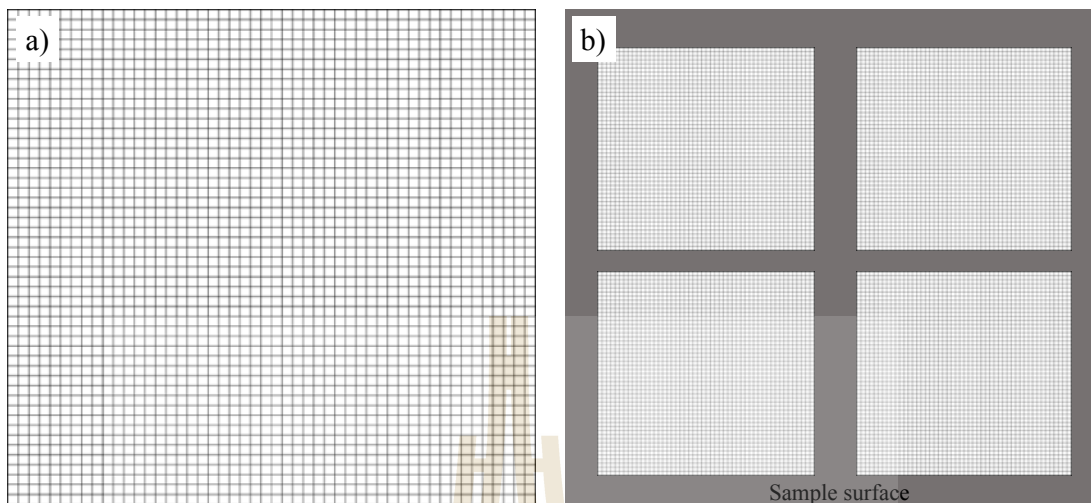


Figure 3.8 a) array pattern of 50 x 50 lines as an ion beam mask for nano pattern preparation. b) 4 masks on the surface of the sample surface.

3.3 Angle resolved photoemission spectroscopy measurement

3.3.1 Nanoscale layered material preparation for ARPES measurement

Sample preparation for measuring ARPES requires particular attention. The sample to be measured must be a single crystal and must have a clean surface because ARPES is a surface-sensitive technique. Typically, the surface cleaning of the bulky material is done under an ultra-high vacuum. For nanoscale layered materials, a nano pattern is created on the surface of the material, which cannot be cleaved off. A different method is required to clean the surface. There are several methods for cleaning the surface of the material, such as ion bombardment (or sputtering) on the surface. This method is suitable for materials that have hard and dirty surfaces, such as transition metal oxide. The sputtered surfaces also cause damage to the surface of the material, which makes it unsuitable for nano patterning. Non-destructive surface cleaning methods are annealing and exposing high-intensity UV rays on the surface under an

ultra-high vacuum. The heat from these methods destroys the organic compounds attached to the surface, making the surface cleaner.

3.3.2 Electronic structure observation

The electronic structure of nano HOPG was observed by angle-resolved photoemission spectroscopy (ARPES). In this measurement, the beam must cover the area of the nano pattern that is approximately 100 x 100 micrometers. The sample surface has a nano-pattern, so it cannot be cleaned by cleaving. Therefore, the surface of the sample was cleaned up by heating or UV irradiation. The results that were taken by ARPES measurement consist of band dispersion at gamma and the edge of the hexagonal Brillouin zone of nano HOPGs pattern, near nano HOPGs pattern, and HOPG substrate. Firstly, we mapped the valence band dispersion to find the direction from gamma to the edge of the hexagonal Brillouin zone. Once the location and direction of the edge were known, we then performed the positioning of the nanopatterns on the surface of the sample. To point at the nano HOPGs array on the HOPG substrate, we specified the position by using the edge of the HOPG substrate as a reference point, then measured the ARPES around the nano array by 12 points as 300 x 400 square micrometers and 100 micrometers as a step size for movement. Moreover, we also observed band dispersion of HOPG substrate that is far from the array by 1 mm. We focused on the Dirac cone near the Fermi level to observe the sample's bandgap opening. The data were collected by three experimental beamlines using a process similar to the one described above. The conditions for the ARPES measurement of each station were as follows:

CASSIOPEE beamline, SOLEIL synchrotron, photon energy was used at 60 eV, the beam spot size on the sample is 40 x 20 to 100 x 100 μm^2 , detector is a Scienta

R4000 with wide-angle lenses, sample temperature was set at 60 K, and energy resolution was held at 15 meV for all experiment. The sample was irradiated UV (synchrotron light) to remove organic compound on the surface. We evaporated potassium as electrons doping on sample surface to observe a top of Dirac cone. Figure 3.9 show ARPES system at CASSIOPEE beamline.

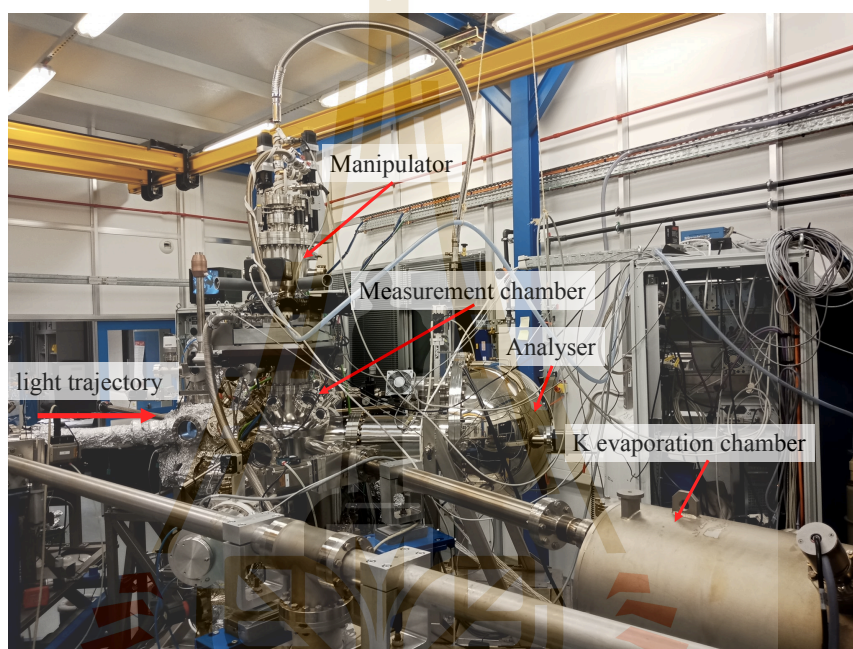


Figure 3.9 ARPES system at CASSIOPEE beamline.

Experimental station 5-2, Stanford Synchrotron Radiation Lightsource, photon energy was used at 60 eV, beam spot size on the sample is 40 (horizontal) x 10 (vertical) μm^2 , detector is a SCIENTA D80 Electron Analyzer, sample temperature was set at 60 K, and energy resolution was held at 15 meV for all experiment. The sample was irradiated UV (synchrotron light) to remove organic compound on the surface.

At beam line 09U1 High Resolution and Wide Energy Range Photoemission Spectroscopy Beamline at Shanghai Synchrotron Radiation Facility, photon energy was used at 95 eV. Detector is Scienta analyzer. The sample was measured by uncleaned

surface and surface of sample was cleaned up by heating at 500 °C under high vacuum. Since pattern area of nano HOPG is 100x100 μm^2 , we used beam spot 20 μm x 30 μm for all of measurement. During ARPES measurement, spectra were collected at 15 K in ultrahigh vacuum (UHV) with a base pressure better than 1×10^{-10} Torr. The energy resolution is better than 15 meV at 95 eV photon energy.

Energy dispersion curve (EDC) of the ARPES spectra were extracted across k_F to compare between nano array and other point on HOPG substrate. To indicate bandgap opening on the sample, the EDC spectra were symmetrized by using Au's Fermi level as a reference.

3.3.3 Symmetrized spectrum

A symmetrical spectrum is used for the probe of narrow energy gaps in materials for the measurement of ARPES. For symmetrical processes, The EDC spectrum is duplicated, and the energy axis is set to the opposite number, with the Fermi energy being the pins. These spectrums are combined. If there is an energy gap, the combined spectrums become a hole where the Fermi energy is compared to if there is no gap, the combined spectrums become flat as shown in figure 3.10.

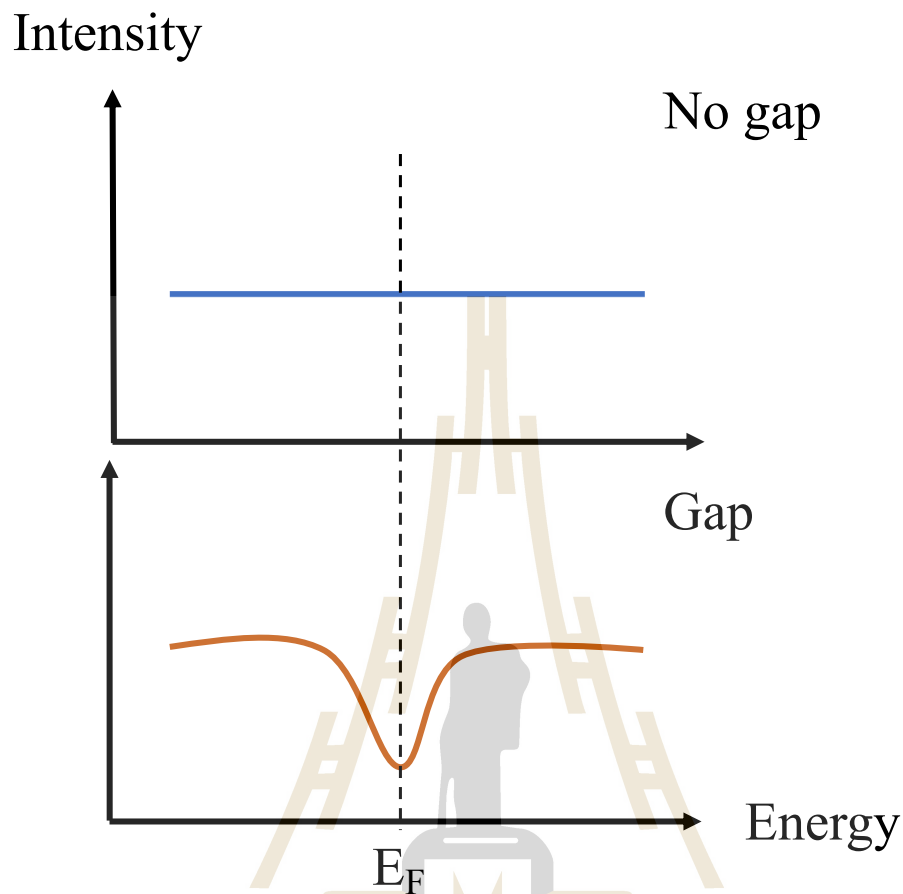


Figure 3.10 The combined spectrums of the case of there are no energy gap and there is energy gap.

Symmetrized spectrum is widely used in energy gap analysis from ARPES measurements, especially with super conductor and narrow gap materials. Yoshida and his team symmetrically analyzed EDC spectrums to observe the super conducting gap of the iron-based superconductor $\text{BaFe}_2(\text{As}_{1-x}\text{P}_x)_2$ at above and below T_c . They found that the complicated gap modulation can be theoretically reproduced by considering both spin and orbital fluctuations (Yoshida et al, 2014). Li and co-worker investigated energy gap of trilayer nickelate $\text{La}_4\text{Ni}_3\text{O}_{10}$ by symmetrized EDCs as a function of temperature. They found that when moving toward higher temperature, the spectral

weight within the energy gap gradually increases and the coherence peaks of the spectra are broadened. Moreover, the energy gap opening is consistent with the phase transition temperature (Li et al., 2017).

3.4 Raman spectroscopy

Raman spectra of nano HOPG and HOPG substrate were observed by using SENTERRA II Dispersive Raman Microscope from Bruker Optics as shown in figure 3.11. Raman spectra were acquired under condition laser wavelength 532 nm, beam size 1 μm , laser power 50 mW.



Figure 3.11 SENTERRA II Dispersive Raman Microscope from Bruker Optics.

D band, G band and 2D band of Raman spectra were characterized and we focused on Raman frequency and FWHM of 2D band that indicated by Lorentzian fitting. Two Lorentzian peaks were used to fit the 2D band Raman spectrum.

3.5 DFT calculation

We carried out theoretical approach based on density functional theory (DFT) in implement of VASP 5.3 code. (Kresse and Furthmüller, 1996) All DFT calculations were taken account into the frozen-core projector augmented wave (PAW) method to correct the electron-ion interaction. (Blöchl, 1994) The exchange correlation functional was explained by Perdew-Burke-Ernzerhof (PBE). (Perdew, Burke and Ernzerhof, 1996) The van der Waals force between graphene layers was considered by DFT+D3 with Grimme approach. (Grimme et al., 2010) The kinetic energy cut off was set to 520 eV for the plane wave basis set. The Brillouin zone integration via the Gaussian smearing method was set a broadening width of 0.001 eV. Note that the calculated band gaps of electronic band structure from PBE approach are systematically underestimate due to the DFT self-interaction error. However, tend of band gap opening based on applying strain are still available to study. The relation of energy gap and percentage of tensile strain was observed by using DFT calculation. Three layers graphene were used as a model for strain calculation. Tensile strain was applied on a top layer of the model in armchair direction. Moreover, two layers graphene was also used for the calculation

CHAPTER IV

RESULTS AND DISCUSSION

The contents of this chapter consist of the morphology of nanoscale crystalline layered materials that describe the characteristics of nanoscale crystalline HOPG. The electronic structure of nanoscale crystalline layered materials was mentioned in the second content, followed by Raman spectroscopy observations. The last content in this chapter is an energy gap opening discussion that will reveal the cause of the bandgap opening of nanoscale crystalline HOPG.

4.1 Morphology of nanoscale crystalline layered materials

The purpose of this study is to fabricate nanocrystalline layered materials using a focused ion beam. The research focused on layered materials, particularly highly oriented pyrolytic graphite (HOPG). The nanocrystalline structure was created on a highly oriented pyrolytic graphite (HOPG) substrate from SpectrumInstrument (HOPG YZA Quality, piece size 7x7 mm., thickness 0.8–1.8 mm.) at Suranaree University of Technology's center for scientific and technological equipment. The nanoscale crystalline in this work is expected to have a square of island on the HOPG substrate, as shown schematically in figure 4.1.

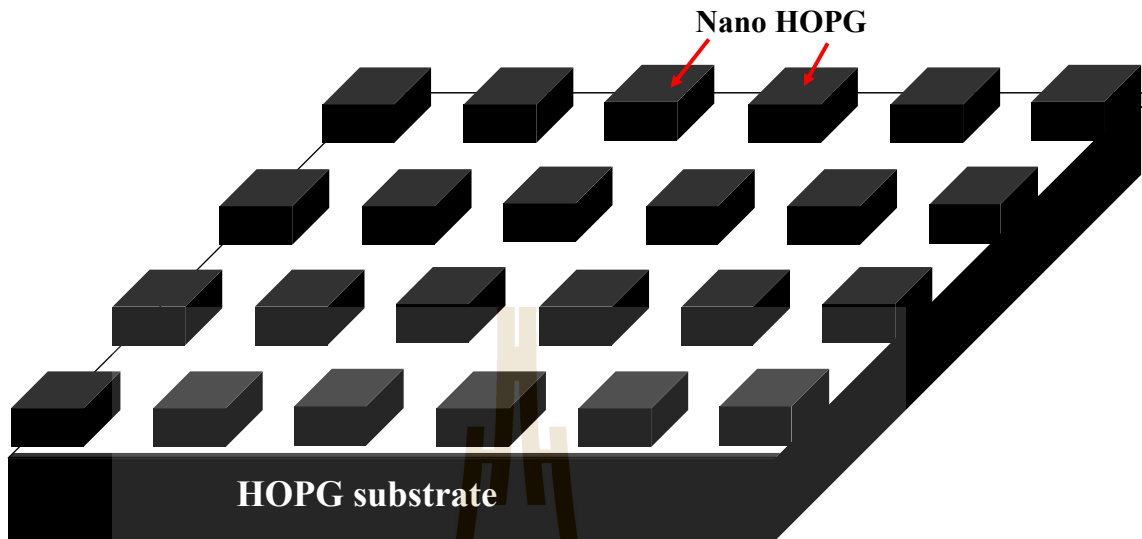


Figure 4.1 Schematic of nano-scale HOPG on HOPG substrate.

Firstly, we used a mask of 100 lines x 100 lines to fabricate nanoscale crystalline on HOPG substrate. Figure 4.2 illustrates a SEM picture of nanoscale crystalline on a HOPG substrate at various magnifications (a is 2,000x and b is 5,000x). The form of nano HOPGs resembles a square or a dot varying size and array of nanoscales on the substrate covered an area of $50 \times 50 \mu\text{m}^2$.

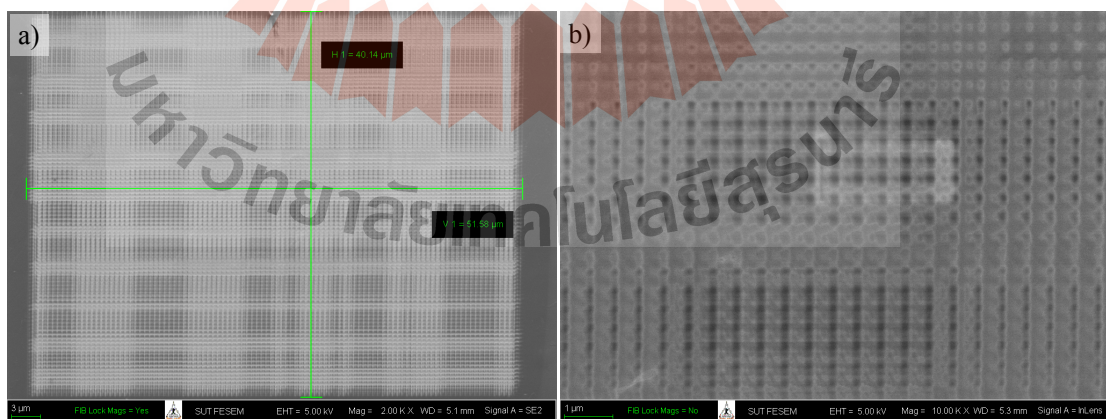


Figure 4.2 SEM picture of nanoscale crystalline on a HOPG substrate as prepared by using a mask of 100 lines x 100 lines a) 2kx and b) 5kx of magnification.

Due to the different shapes and sizes, we therefore used new conditions for the preparation of nanocrystalline. We applied a 50 x 50 line mask to produce nanoscale crystalline and placed it in four locations on a HOPG substrate. Figure 4.3 shows a SEM image of nanoscale crystalline on a HOPG substrate produced with the use of such a mask. By using such a condition, we can obtain a homogeneous pattern on the substrate as shown in figure 4.3 a. At the nanoscale, nano HOPGs have the shape of a square island, and the array on the substrate covers an area of about 100 x 100 nm². Nanocrystalline structures with a diameter of 500 nm and 300 nm, as illustrated in figures 4.3 b and c, respectively, were produced using various FIB magnifications. For example, nanocrystalline size is dependent on FIB magnification; for example, nanocrystalline with a diameter of 500 nm requires 750 times magnification, whereas a diameter of 300 nm requires 1000 times magnification. Moreover, the array of nano HOPGs will still be in the same crystalline orientation as the original substrate.



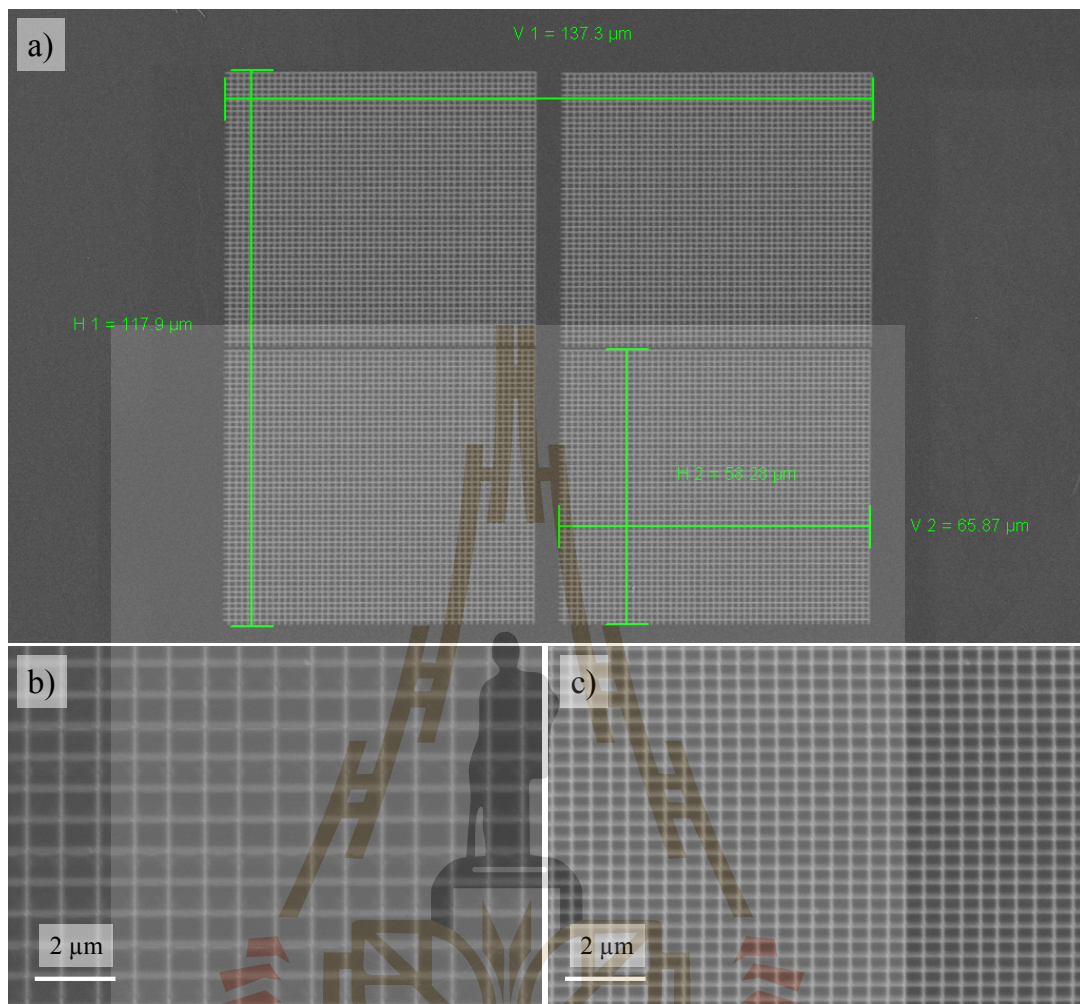


Figure 4.3 SEM picture of nanoscale crystalline on a HOPG substrate as prepared by using a mask of 50 lines x 50 lines placed it in four locations on a HOPG substrate. a) The array on substrate cover area approximately $100 \times 100 \mu\text{m}^2$. b) Nanocrystalline structures with a diameter of 500 nm. c) Nanocrystalline structures with a diameter of 300 nm.

4.2 Electronic structure of nano scale crystalline layered materials

Angle-resolved photoemission spectroscopy (ARPES) was used to investigate the electronic structure of highly orientated pyrolytic graphite (nano HOPG). Because HOPG is azimuthally disordered, its Fermi surface is a circle (schematic red dash line) oriented on the Brillouin zone (blue solid line). While HOPG is more disordered azimuthally than graphite, its band dispersion is invariant with azimuthal angles (Zhou et al., 2005). As a result, the band dispersion along the red arrow in figure 4.4 a stays unchanged with azimuthal angle. Figure 4.4 b illustrates the valence band dispersion of HOPG as seen along the red arrow in figure 4.4 a. We focused on Dirac cone near Fermi level as show in insert figure in figure 4.4 b to observe bandgap opening of the sample.

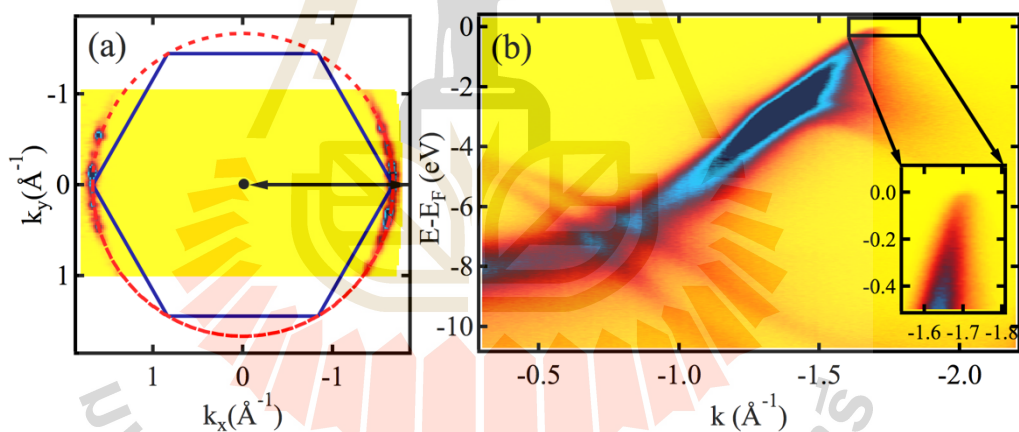


Figure 4.4 a) Electronic structure of highly orientated pyrolytic graphite (HOPG) consist of Fermi surface map of HOPG. b) Band dispersion along black arrow in figure a) and insert figure is band dispersion near Fermi level in black solid box.

The electronic structure of nanoscale crystalline highly orientated pyrolytic graphite (nano HOPG) produced with a mask of 100 lines x 100 lines was observed at the CASSIOPEE beamline, SOLEIL synchrotron, France. We examined the bandgap

opening at the edge of the HOPG Brillouin zone. The HOPG sample was classified into two types: normal HOPG, which represents the crystalline HOPG substrate, and nano HOPG, which represents the nanoscale crystalline HOPG. The measurement was performed on an uncleaved sample that had been cleansed with UV irradiation. The samples were measured at 60 K, with a resolution of 15 meV and a photon energy of 60 eV. The top of the Dirac cone cannot be found in its normal state, as shown in figure 4.5 a. However, by evaporating Cs metal, electrons from Cs are donated to the HOPG surface, resulting in electrons filling up at the top of the Dirac cone. As shown in figure 4.5 b, the Dirac cone of HOPG was detected 5 minutes after Cs was evaporated.

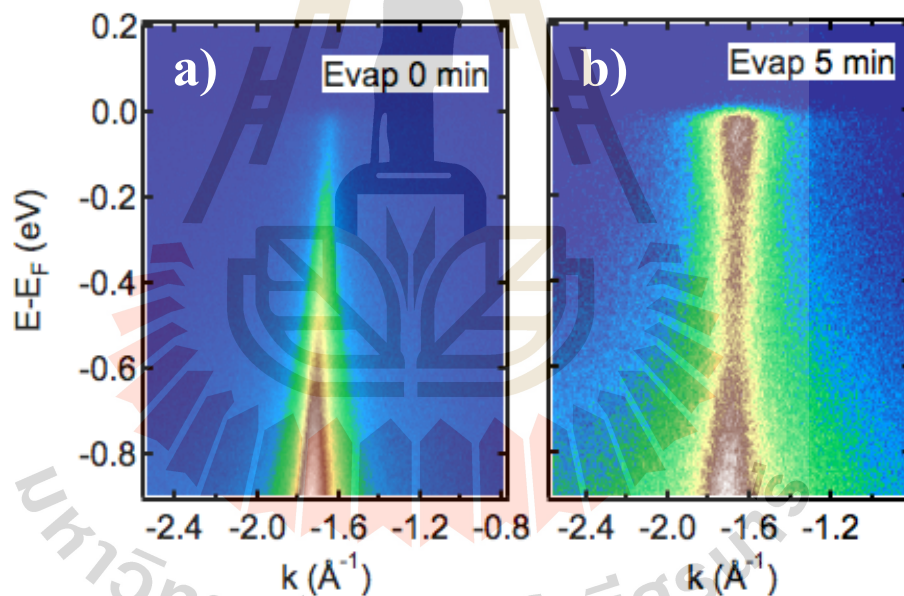


Figure 4.5 a) and b) Band dispersion near Fermi level of HOPG which were evaporated Cs 0 minute and 5 minutes, respectively.

Figure 4.6 a and b illustrate the Dirac cones of nano HOPG and normal HOPG, respectively. The energy dispersion curve (EDC) spectra of nano HOPG and normal HOPG were extracted throughout the k_F of the Dirac cone and are shown in figure 4.6

c. Normally, the density of state at the Dirac point is represented by the EDC spectrum of normal HOPG (blue arrow and text in figure 4.6 c, indicating that the bandgap remains closed). The density of state of the Dirac point vanishes in nano HOPG, indicating that the bandgap of nano HOPG has been opened to an estimated 0.285 eV.

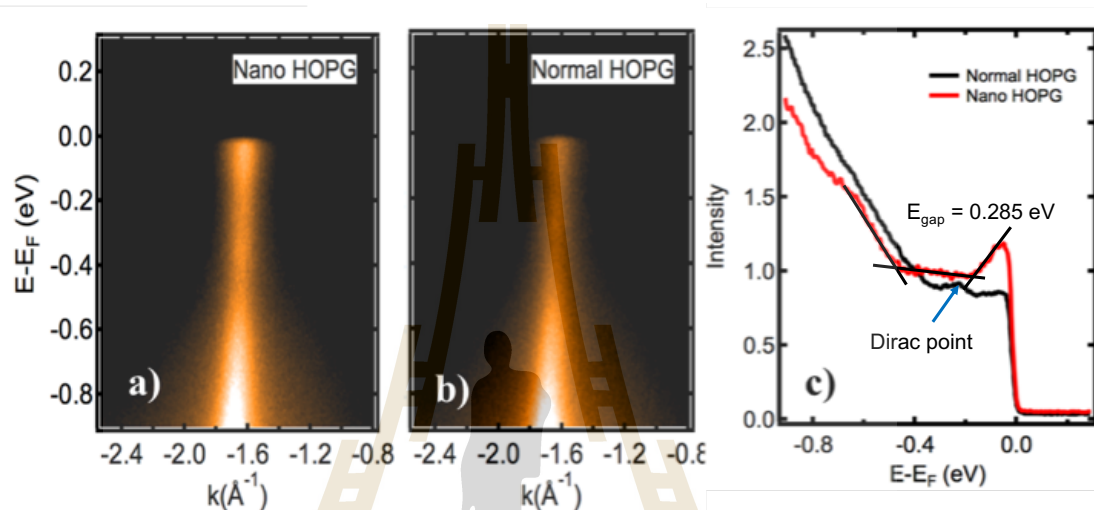


Figure 4.6 Dirac cone (a. and b.) and spectral weight of nano HOPG and normal HOPG (c.). EDC spectrum of nano HOPG exhibit bandgap opening 0.285 eV and Dirac point of normal HOPG indicated by blue arrow and text.

The change of the Dirac point may be readily seen as a result of electron doping with alkali metals evaporation. However, such processes have a direct effect on the electrical structure of the layered material, such as the electric field induced by potassium doping in bilayer graphene (Ohta et al., 2006) or the indirect to direct bandgap transition of MoS_2 caused by potassium intercalation (Eknapakul et al., 2014). Therefore, the measurements without alkaline metal evaporation can rule out the effects of alkali metals to band gap at Dirac point. Electronic structure of nano HOPG produced with four mask of 50 lines x 50 lines was observed at Experimental station 5-2, Stanford Synchrotron Radiation Lightsource for 500 nm of nano HOPG and 09U1 High

Resolution and Wide Energy Range Photoemission Spectroscopy Beamline at Shanghai Synchrotron Radiation Facility for 300 nm of nano HOPG. To find nanoscale crystalline position on HOPG substrate, ARPES spectrums were measured as a position mapping. Figure 4.7 a. show position mapping on HOPG substrate in $100 \times 100 \mu\text{m}^2$ area per step. EDCs at k_F of ARPES spectrum of each position were symmetrized to find bandgap opening as shown in figure 4.7 b. The symmetrized EDCs spectrum were used to observe gap opening in superconductor. (Yoshida et al., 2014) Symmetrized spectrums of position 5, 6 and 9 in figure 4.7 b show bandgap opening around 160 meV. This indicate that nanoscale crystalline position on HOPG substrate was indicated as position 5, 6 and 9.

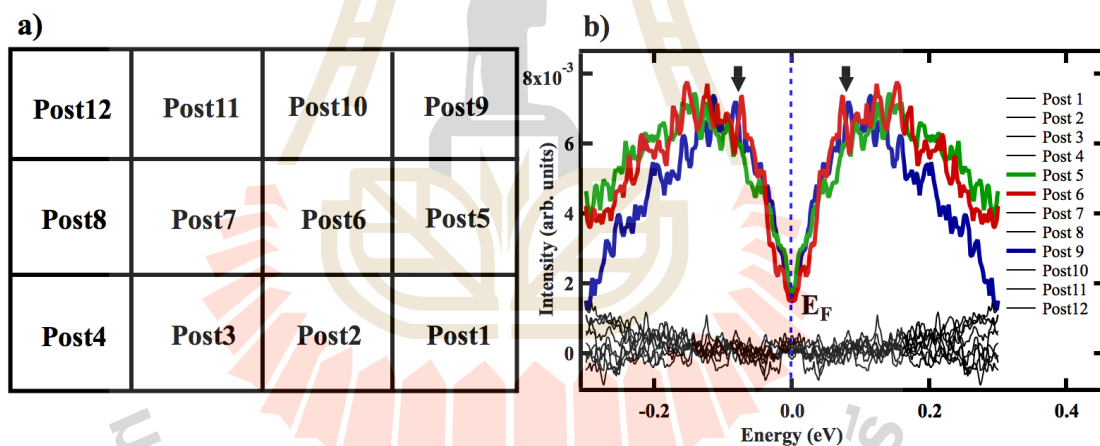


Figure 4.7 a) position mapping in $100 \times 100 \mu\text{m}$ per step and b) Symmetrization spectrums of EDCs at k_F of ARPES spectrum of each position.

Figure 4.8 a and b show symmetrized ARPES spectra of nanoscale crystalline HOPG with crystalline diameters of 500 nm and normal HOPG, respectively. The measurements were made at Stanford Synchrotron Radiation Lightsource Experimental Station 5-2. The bandgap is visible in figure 4.8 a but vanishes in figure 4.8 b. To

determine the size of the bandgap, EDC spectra across K_F were extracted, as shown in figure 4.8 c. By comparing HOPG's Fermi level (E_F) to gold, the Fermi level (E_F) was adjusted. As illustrated in figure 4.8 d, the bandgap of nanoscale crystalline HOPG was found to be approximately 160 meV when the spectra were symmetrized.

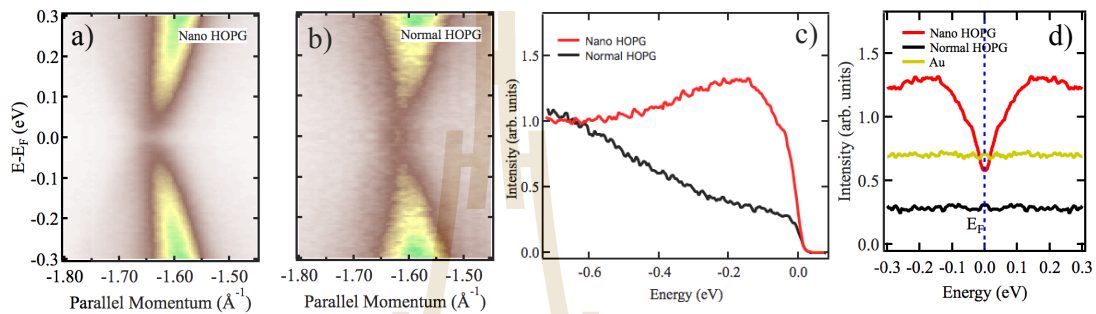


Figure 4.8 a) and b) Symmetrized ARPES spectra of nanoscale crystalline HOPG with crystalline diameters of 500 nm and normal HOPG, respectively. c) EDC spectra across K_F of nanoscale crystalline HOPG and normal HOPG. d) Symmetrized of c) that Fermi level is referenced with gold.

The electronic structure of nano HOPG with a diameter of 300 nm was observed by angle resolved photoemission spectroscopy (ARPES) at beam line 09U1: High Resolution and Wide Energy Range Photoemission Spectroscopy Beamline. ARPES spectra were explored in 3 different areas, consisting of HOPG substrate, near nano-HOPG pattern, and nano-HOPG pattern. Figure 4.9 a, b, c, and d show ARPES spectra of the HOPG substrate, near nano HOPG pattern, nano HOPG pattern, and Au, respectively. Nano HOPG reveals the state below Fermi level that disappears in normal HOPG and this state was found for three measurements in different samples. This state was made clear by energy dispersion curve (EDC) spectra that were extracted across k_F as shown in figure 4.9 i-l. Normally, graphene or graphite have a Dirac cone at the K

point of the Brillouin zone, and the Dirac point is located at Fermi level. So, the state that occurred below Fermi level on nano array HOPG indicated that there was a gap opening on nano HOPG. The gap opening on the nano array HOPG is clearly seen by symmetrized ARPES spectra using Au's Fermi level as a reference. Figure 4.9 e-h shows symmetrized ARPES spectra of HOPG substrate near nano HOPG pattern and nano HOPG pattern, respectively. The EDC spectra of these symmetrized ARPES spectra shown in figure 4.9 m-p revealed the gap opening is approximately 90 meV as shown in figure 4.9 m.

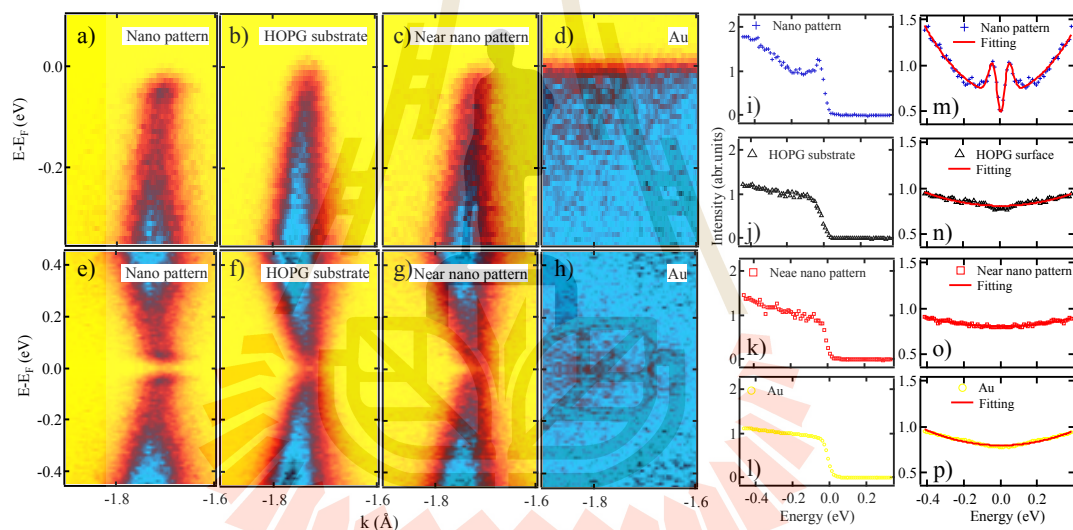


Figure 4.9 a) – d) ARPES spectra of nanoscale HOPG pattern, HOPG substrate, near nanoscale HOPG pattern, and Au respectively. e) – h) symmetrized ARPES spectra of nanoscale HOPG pattern, HOPG substrate, near nanoscale HOPG pattern, and Au respectively. i) – l) Energy dispersion curve (EDC) spectra across k_F of ARPES spectra of nanoscale HOPG pattern, HOPG substrate, near nanoscale HOPG pattern, and Au respectively. m) – p) Symmetrized energy dispersion curve (EDC) spectra across k_F of ARPES spectra of nanoscale HOPG pattern, HOPG substrate, near nanoscale HOPG pattern, and Au respectively.

Bandgap openings can be seen on nano HOPGs of all sizes, as shown in the output above. We would like to know what is causing the nano HOPG bandgap. One of the things that we are interested in is the process of preparing the nano pattern and whether it affects the nano HOPG bandgap, which we will discuss in the next section.

4.3 Raman spectroscopy observation

Researchers studied the effect of an ion beam that was irradiated on the sample surface on the crystallographic structure of HOPG. The ion beam created an edge of a nano hole or nano island that was dominated by a zigzag edge (Girit et al., 2009; Krauss et al., 2010). Moreover, the ion beam is the cause of the disordered structure that was directly observed by the Raman technique. The disorder structure depends on the density of ion dose, and the HOPG surface becomes amorphous at high ion dose (Archanjo et al., 2011; Rodriguez et al., 2019). There is work currently presenting a metallic-to-semiconducting transition in multilayer graphene by using an ion beam to create nano holes (Thiyagarajan et al., 2015). Therefore, the energy gap induced by the ion beam was considered. In this work, Raman spectra of nanoscale HOPG pattern, HOPG substrate, and near nanoscale HOPG pattern were observed as shown in figure 5.10. As shown in the black spectrum, the Raman spectrum of the HOPG substrate reveals a perfect sp^2 structure of graphite with no disorder peak. The Raman spectra of the nanoscale HOPG pattern (blue) and the near nanoscale HOPG pattern (red) clearly show a disorder peak caused by ion beam sputtering. The disorder peak and G peak of the nanoscale HOPG pattern are quite broad due to the high ion doses obtained during

nanoscale production, but the nanoscale remains crystalline, as shown by the shape peak at the top of the G peak in the inset image.

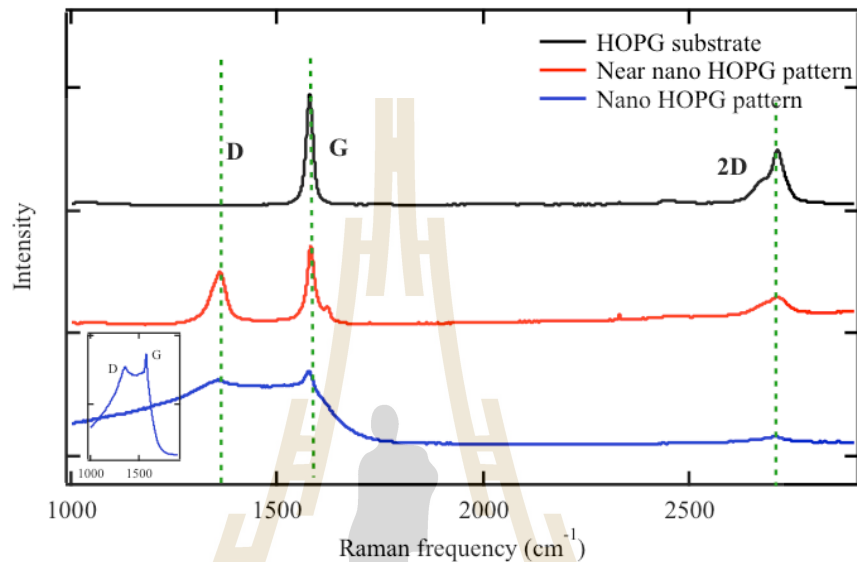


Figure 4.10 Raman spectra of nanoscale HOPG pattern (blue), HOPG substrate (black), and near nanoscale HOPG pattern (red). Inset figure is zoom in D and G peak of nano HOPG Raman spectrum.

In this experiment, we directly observed the energy gap of the nano array HOPG by using the ARPES technique. Normally, the ARPES data should come from a single crystal sample. Hence, disordered structure is not the cause of the energy gaps. Moreover, we also proved a relationship between disorder structure and gap opening. The disorder peak (D peak) of nano HOPG and the neighboring area, as shown in blue and red solid lines in figure 4.10, reveal disorder defects caused by ion beam sputtered but disappear in the HOPG surface, as shown in black solid line in figure 5.10. Symmetrized ARPES spectra of these regions, shown in figures 4.9 e-g, reveal that there is a gap of only nano HOPG and it disappears on the neighboring normal HOPG

surface. This result demonstrates that an ion beam can't induce an energy gap in this work.

To carry out a thorough study of the Raman spectrum, the D mode, G mode, and 2D mode of the Raman spectra were characterized. Specific data such as peak location and FWHM are unreliable due to the broad spectrum of D and G modes. As a result, the 2D mode was utilized for specific data analysis in this study. Lorentzian fitting was used to characterize the 2D mode of Raman spectra. The 2D peak of the Raman spectrum was divided by two Lorentzian peaks according to the equation below (Ferrari et al., 2006)

$$f(x) = y_0 + y_1x + \left(\frac{A_1 F_1^2}{2(x-x_1)^2 + F_1^2} \right) + \left(\frac{A_2 F_2^2}{2(x-x_2)^2 + F_2^2} \right) \quad (4.1)$$

whereas A is amplitude, F is Full Width at Half Maximum (FWHM), x with subscript is peak position $y_0 + y_1x$ is linear background. The subscript numbers denote the first and second peaks of the 2D mode, respectively. Figure 4.11 shows a 2D Raman spectral mode fitted with the above equation.

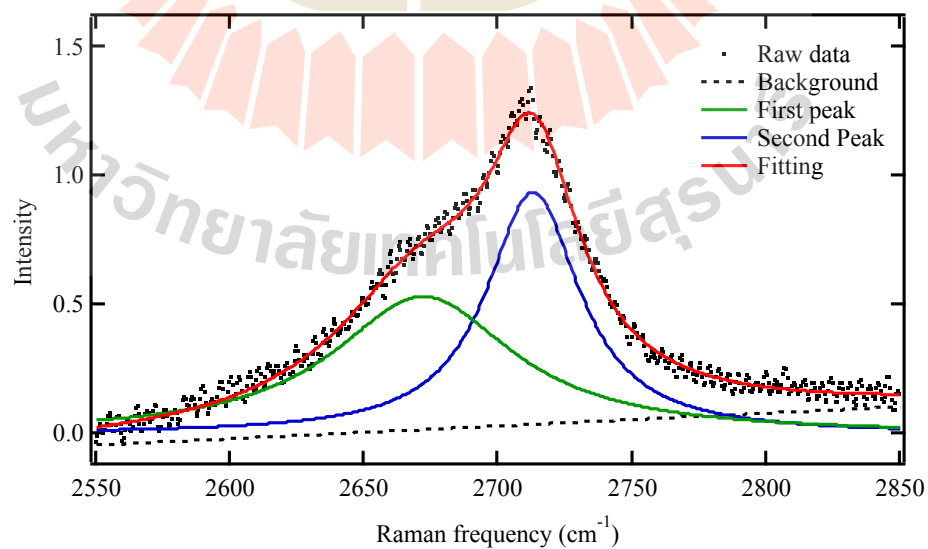


Figure 4.11 2D mode Raman spectrum with two peaks of Lorentzian fitting and linear background.

According to fitting, the first peak has a larger FWHM than the second and a lower amplitude than the second. The second peak is dominant in two-dimensional mode and was utilized to determine the peak location in two-dimensional mode. The peak point of the 2D mode Raman spectroscopy is a critical parameter for determining what is occurring at the nanoscale crystalline, as discussed in the next section.

4.4 Energy gap opening discussion

To discuss the gap opening on nanoscale crystalline HOPG, there are many effects that can be caused by this evidence. The quantum confinement effect is the first candidate to explain the gap opening because of the nano-scale of the sample. Normally, nano-sized graphite-based materials can be semi-conductor materials due to a bandgap caused by the quantum confinement effect. The shrinking of the bandgap depends on the size extension of the nanoparticle. This effect is dominant in the electronic structure of a few-nanometer particle (Kim et al., 2012). In Figure 4.12, the bandgap of graphene quantum dots (GQDs) is compared to the bandgap of nano HOPG. The red transparent squares show bandgaps of the nano HOPG from the experiment compared with the solid black lines based on the work of Ritter and Lyding, 2009. In their work, the energy gap of nano array HOPG is larger than other graphene-base nanoscale (GQD, GNR) at the same size, up to 1 orders of magnitude (Ritter and Lyding, 2009). Therefore, the quantum confinement effect is not mainly affected on gap opening of nano array HOPG.

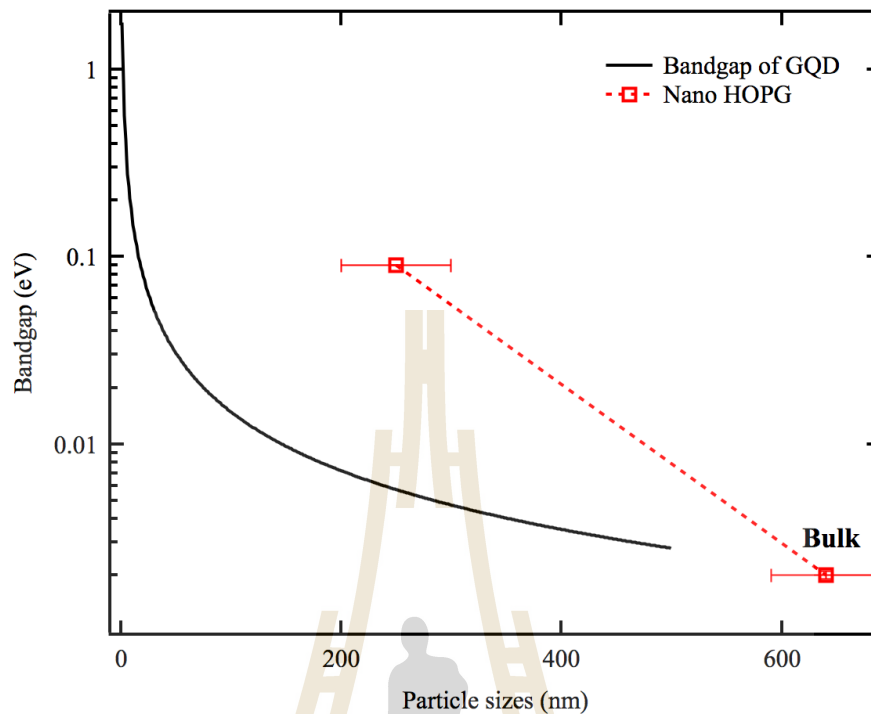


Figure 4.12 Bandgap of graphene quantum dots (GQDs) is compared to the bandgap of nano HOPG (this graph was modified from Ritter and Lyding, 2009).

The second effect that we consider is the edge structure of nano-scale graphite material. The edge of nano-scale graphite material is significantly influenced by electronic structure. The energy gap of graphene nanoribbons (GNRs) of similar width is different as unlike edges (zigzag edge and armchair edge), but this effect is still minor when considered with quantum confinement efficiency (Ritter and Lyding, 2009). However, by the ion beam sputtered process, the edge or vacancies of the nano graphite-base may be bound with some organic compound that causes a metallic to semiconductor transition (Thiyagarajan et al., 2015). The organic bounding of nano graphite-base has an effect on the vibrational frequency of molecules that was indicated by a shift in the Raman frequency of the vibrational mode. C-C bond in G mode and 2D mode are in-plane vibrational modes. As has been observed in graphene oxide and

graphite, the wave number of G mode and 2D mode are shifted to a higher wave number due to the oxygenation of graphite (Perumbilavil et al., 2015). The Raman spectra of the nanoscale HOPG pattern (blue), the HOPG substrate (black), and the near nanoscale HOPG pattern (red) as shown in figure 4.13 a were characterized by Lorentzian fitting. The 2D peak of the Raman spectrum was divided by the first and second Lorentzian peaks. By Lorentzian fitting, the peak position of the second peak of the nanoscale crystalline HOPG is significantly redshifted, which is 4 cm^{-1} compared to the HOPG surface, as shown in figure 4.13 b. The redshift refers to the decreasing oscillation frequency of the 2D mode, which may confirm that the organic bonding is not dominated by nano HOPG. Moreover, there is a possibility that this redshift may come from the expansion of the carbon hexagonal ring, which is called tensile strain (Ni et al., 2008).

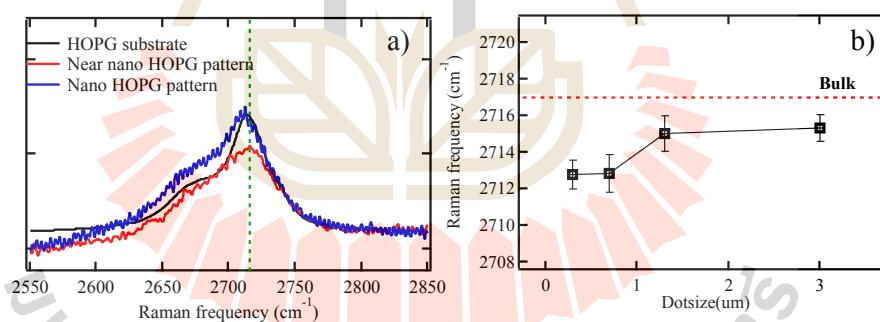


Figure 4.13 a) 2D mode of Raman spectra of nanoscale HOPG pattern (blue), HOPG substrate (black), and near nanoscale HOPG pattern (red). b) Peak position of second peak of 2D mode Raman spectra of bulk and nanoscale crystalline HOPG.

To understand the strain dependence of the electronic structure of graphene-based materials, we carried out first-principle electronic band structure calculations of graphene under a biaxial tensile strain. The relaxed structural unit cell of trilayer

graphene was used for simulation multi-layer effect of graphene in HOPG, as shown in figure 4.14 a. In order to study band-gap opening, we considered the electronic band structure of trilayer graphene compared with monolayer graphene in the presence of biaxial tensile strain varying from 0 to 2% according to the schematic as shown in figure 4.14 b. From the experimental result, the Raman spectra of the 2D peak are shifted to lower frequency relating to the increase of the C-C bond length. In addition, the Raman 2D band corresponds with the $iTO (A_1)$ phonon modes in D_{3h} symmetry, in which all carbon atoms on the carbon ring move towards and move outward the Γ -center. Therefore, the biaxial tensile is a possible type of strain that corresponds with 2D band vibration mode and plays an important role in expanding C-C bond length in all directions. The comparative energy gap as a function of biaxial tensile strain is depicted in figure 4.14 c. Note that the calculated energy gaps of graphene with applied strain are lower than the experimental values due to the common self-interaction error of DFT-PBE calculation. The finding shows that the energy gap of monolayer graphene tends to linearly increase, whereas that of trilayer graphene is roughly increasing. The band structure of trilayer graphene in the absence of strain is shown in figure 4.14 e. During applied 0 to 2% strain, computational investigation reveals that the highest gap opening of trilayer graphene is under 1.1% strain with an energy gap of 93.0 meV, which is close to the measured energy gap of HOPG (112 meV). Meanwhile, that of monolayer graphene is equal to 80.9 meV, which is lower. The corresponding band structure at K-point is illustrated in figures 4.14 d and 4.14 f for monolayer and trilayer graphene at 1.1% strain, respectively. According to this computational result, it suggests that the biaxial tensile strain of trilayer graphene is likely responsible for the gap opening of HOPG.

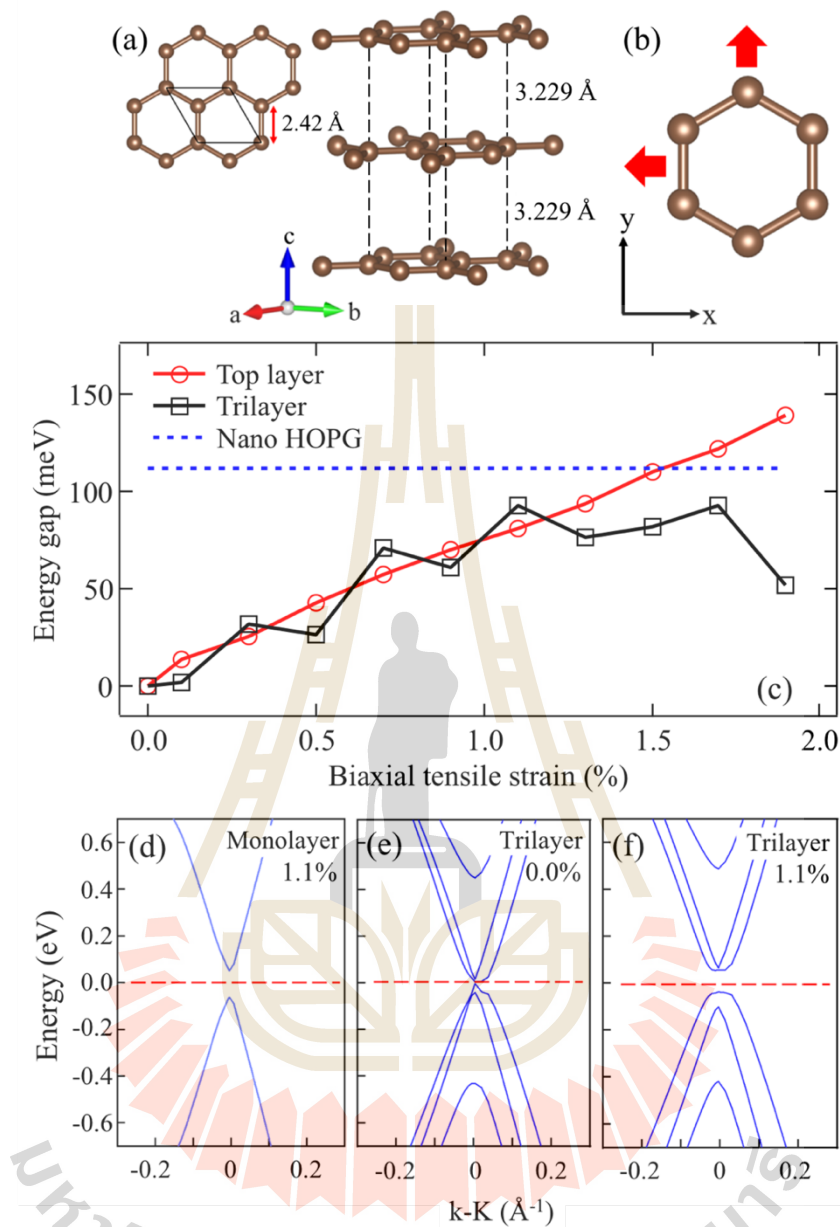


Figure 4.14 (a) The geometric structure of trilayer graphene with corresponding C-C bond distance and the interlayer spacing. (b) Schematic of biaxial tensile strain with a same strain value along x- and y-direction. (c) The comparative energy gap of monolayer, trilayer graphene, and nano HOPG. The corresponding band structure of monolayer graphene with applied 1.1% strain (d), trilayer graphene with no strain (e), and trilayer graphene with applied 1.1% strain (f).

In this study, we found that the bandgap of nanoscale crystalline exists in the hundreds of meV range, which corresponds to the energy range from mid-infrared to terahertz. In comparison to previous research that found bandgaps in single crystal graphene, the bandgaps created by the various methods are identical in the hundreds of meV range. For example, an electric field generated in bilayer graphene results in a bandgap of 250 meV (Ohta et al., 2006; Zhang et al., 2009), whereas graphene grown on a SiC substrate has a bandgap of 260 meV for a single layer and decreases with the number of layers (Zhou et al., 2007). Additionally, it is effective when the tensile strain of graphene with a bandgap of 300 meV at 1% tensile strain is calculated, and the energy gap reduces as the number of layers rises with the same tensile strain (Ni et al., 2008). As a result, the bandgap of nanoscale crystalline determined in this study is comparable to that of graphene crystalline determined in previous research investigations.



CHAPTER V

CONCLUSIONS

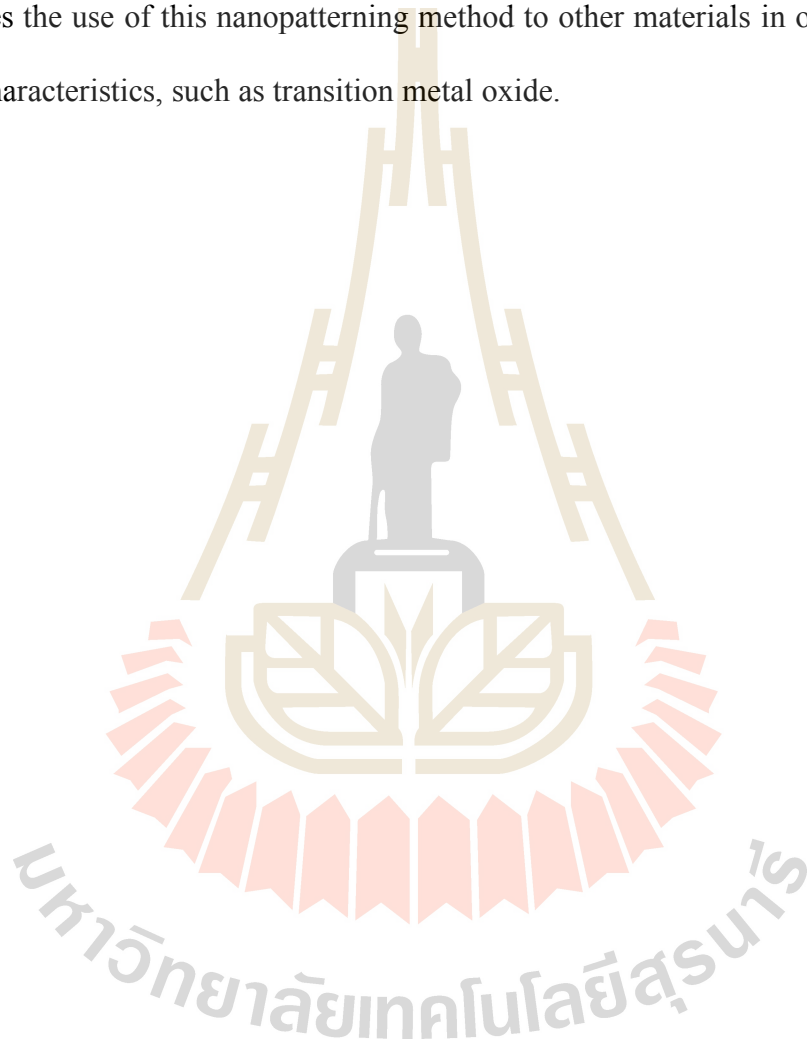
5.1 Conclusions

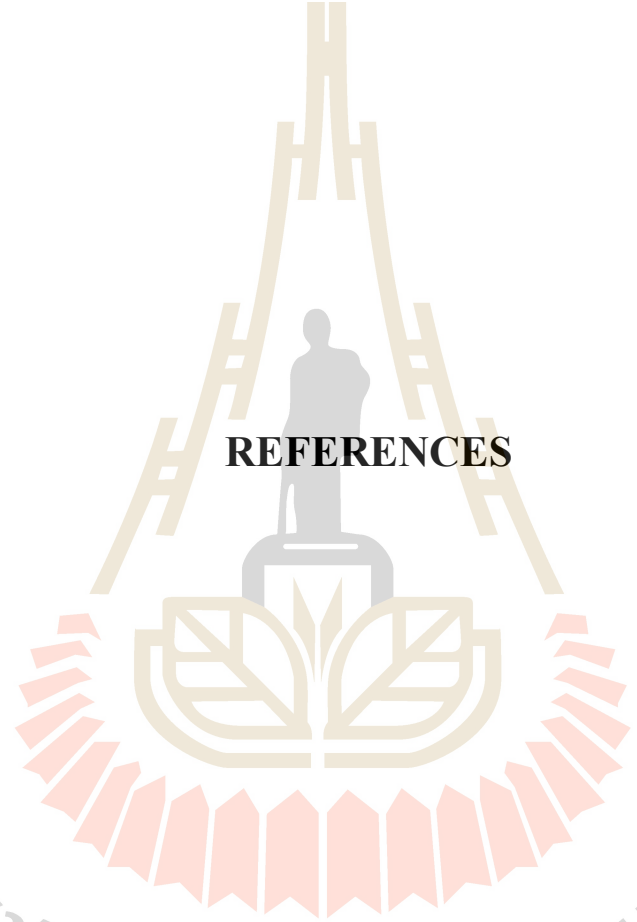
In summary, we need to investigate crystalline layered materials in this work, particularly carbon-based materials such as graphene and graphite, since they have shown tremendous promise for next-generation electrical devices. The fascinating property of graphene that is critical for optoelectronic devices is carrier multiplication, which means that a single photon may create many charge carriers through the Auger process. However, one of the drawbacks of this material is its lack of bandgap. We need to create a bandgap of carbon-base material by cutting it down to the nanoscale. The electrical structure of nanoscale crystalline highly oriented pyrolytic graphite (HOPG) was investigated in this study. HOPG is a two-dimensional carbon-base material that was produced by ion beam sputtering. The nanoscale crystalline HOPGs have the form of a square island on a 100 x 100 micrometer square substrate. Additionally, the array of nano HOPGs must retain the original substrate's crystalline orientation. The energy gap of nano HOPG was determined using angle-resolved photoemission spectroscopy (ARPES). The gap-opening energy of nanoscale HOPG was determined to be in the hundreds of meV range using a symmetrical ARPES spectrum. To demonstrate the gap opening, strain is a possible explanation for this outcome. A Lorentzian fitting of the Raman spectra of nanoscale HOPG reveals a substantial redshift in the peak location of the 2D mode relative to the HOPG surface. The redshift indicates a decrease in the

frequency of the 2D mode, indicating that organic bonding is not dominant on nano HOPG. Additionally, there is a hypothesis that this redshift is caused by the expansion of the carbon hexagonal ring, a process known as tensile strain. To better understand the strain dependence of the electronic structure of graphene-based materials, we calculated the electronic band structure of graphene under uniaxial tensile strain using first-principles calculations. The findings of this computation indicate that the likelihood of gap opening is very compatible with the experimental data. The bandgap of nanoscale crystalline was discovered to be in the hundreds of meV range, which corresponds to the energy range from mid-infrared to terahertz. As an outcome, the bandgap of nanoscale crystalline found in this work is similar to the bandgap of graphene crystalline already determined. This discovery demonstrates how to build a high-purity single crystalline nanopattern and also how to control the energy gap of single crystalline graphite-base materials in order to create high-performance optoelectronic devices. By the way, spintronic and optoelectronic applications need the use of single crystalline materials due to their lack of defects such as grain boundaries, inhomogeneous strain, and dislocations. This absence confers unique properties on single crystals, particularly mechanical, optical, and electrical properties that are dependent on the crystallographic structure. Additionally, single crystalline materials have a high degree of spin and charge polarization alignment, which is beneficial for optoelectronic and spintronic devices.

5.2 Future direction

The next interesting work will be to investigate the electrical structure of layered materials other than HOPG, such as transition metal dichalcogenide (TMDs) with a bandgap and MXenes material with outstanding supercapacitor characteristics. This involves the use of this nanopatterning method to other materials in order to improve their characteristics, such as transition metal oxide.





REFERENCES

มหาวิทยาลัยเทคโนโลยีสุรนารี

REFERENCES

- Archanjo, B. S., Maciel, I. O., Ferreira, E. M., Peripolli, S. B., Damasceno, J. C., Achete, C. A., and Jorio, A. (2011). Ion beam nanopatterning and micro-Raman spectroscopy analysis on HOPG for testing FIB performances. **Ultramicroscopy**. 111(8): 1338-1342.
- Bai, K. K., Zhou, Y., Zheng, H., Meng, L., Peng, H., Liu, Z., Nie J. C., and He, L. (2014). Creating one-dimensional nanoscale periodic ripples in a continuous mosaic graphene monolayer. **Physical review letters**. 113(8): 086102.
- Berger, C., Song, Z., Li, X., Wu, X., Brown, N., Naud, C., Tianbo, M. D., Li, T., Hass, J., Marchenkov, A. N. Conrad, E. H., First, P. N., and de Heer, W. A. (2006). Electronic confinement and coherence in patterned epitaxial graphene. **Science**. 312(5777): 1191-1196.
- Blöchl, P. E. (1994). Projector augmented-wave method. **Physical review B**. 50(24): 17953.
- Brey, L., and Fertig, H. A. (2006). Electronic states of graphene nanoribbons studied with the Dirac equation. **Physical Review B**. 73(23): 235411.
- Castro, E. V., Novoselov, K. S., Morozov, S. V., Peres, N. M. R., Dos Santos, J. M. B. L., Nilsson, J., Guinea, F., Geim, A. K., and Neto, A. H. C. (2007). Biased bilayer graphene: semiconductor with a gap tunable by the electric field effect. **Physical review letters**. 99(21): 216802.

- Cocco, G., Cadelano, E., and Colombo, L. (2010). Gap opening in graphene by shear strain. **Physical Review B**. 81(24): 241412.
- Cooper, D. R., D'Anjou, B., Ghattamaneni, N., Harack, B., Hilke, M., Horth, A., Majlis N., Massicotte M., Vandsburger L., Whiteway E., and Yu, V. (2012). Experimental review of graphene. **International Scholarly Research Notices**. 2012.
- Eda, G., Lin, Y. Y., Mattevi, C., Yamaguchi, H., Chen, H. A., Chen, I. S., Chen C. W., and Chhowalla, M. (2010). Blue photoluminescence from chemically derived graphene oxide. **Advanced materials**. 22(4): 505-509.
- Eknapakul, T., King, P. D. C., Asakawa, M., Buaphet, P., He, R. H., Mo, S. K., Takagi, H., Shen, K. M., Baumberger, F., Sasagawa, T., Jungthawan, S., and Meewasana, W. (2014). Electronic structure of a quasi-freestanding MoS₂ monolayer. **Nano letters**. 14(3): 1312-1316.
- Ferrari, A. C., Meyer, J. C., Scardaci, V., Casiraghi, C., Lazzeri, M., Mauri, F., Piscanec, S., Jiang, D., Novoselov, K. S., Roth, S., and Geim, A. K. (2006). Raman spectrum of graphene and graphene layers. **Physical review letters**. 97(18): 187401.
- Fuhrer, M. S. (2013). Critical mass in graphene. **Science**. 340(6139): 1413-1414.
- Fukushima, S., Shimatani, M., Okuda, S., Ogawa, S., Kanai, Y., Ono, T., and Matsumoto, K. (2018). High responsivity middle-wavelength infrared graphene photodetectors using photo-gating. **Applied Physics Letters**. 113(6): 061102.

- Geim, A. K. and Novoselov, K. S. (2007). The rise of graphene. **Nature Materials**. 6: 183.
- Girit, Ç. Ö., Meyer, J. C., Erni, R., Rossell, M. D., Kisielowski, C., Yang, L., Park, C. Crommie, M. F., Cohen, M. L., Louie, S. G., and Zettl, A. (2009). Graphene at the edge: stability and dynamics. **Science**. 323(5922): 1705-1708.
- Graves, P. R. G. D. J., and Gardiner, D. (1989). Practical raman spectroscopy. **Springer**.
- Grimme, S., Antony, J., Ehrlich, S., and Krieg, H. (2010). A consistent and accurate ab initio parametrization of density functional dispersion correction (DFT-D) for the 94 elements H-Pu. **The Journal of chemical physics**. 132(15): 154104.
- Gui, G., Morgan, D., Booske, J., Zhong, J., and Ma, Z. (2015). Local strain effect on the band gap engineering of graphene by a first-principles study. **Applied Physics Letters**. 106(5): 053113.
- Hertz, H. (1887). Ueber den Einfluss des ultravioletten Lichtes auf die elektrische Entladung. **Ann. Phys.** 267: 983.
- Huñner, S. (1995). Photoemission spectroscopy. Berlin: **Springer-Verlag**.
- Ju, L., Geng, B., Horng, J., Girit, C., Martin, M., Hao, Z., Bechtel, H. A., Liang, X., Zettl, A., Shen, Y. R., and Wang, F. (2011). Graphene plasmonics for tunable terahertz metamaterials. **Nature nanotechnology**. 6(10): 630-634.
- Kim, J. H., Lee, J., Kim, J. H., Hwang, C. C., Lee, C., and Park, J. Y. (2015). Work function variation of MoS₂ atomic layered grown with chemical vapor

deposition: The effects of thickness and the adsorption of water/oxygen molecules. **Applied Physics Letters**. 106(25): 251606.

Kim, S., Hwang, S. W., Kim, M. K., Shin, D. Y., Shin, D. H., Kim, C. O., Yang, S. B., Park, J. H., Hwang, E., Choi, S. H., Ko, G., Sim, S., Sone, C., Choi, H. J., Bae, S., and Hong, B. H. (2012). Anomalous behaviors of visible luminescence from graphene quantum dots: interplay between size and shape. **ACS nano**. 6(9): 8203-8208.

Krauss, B., Nemes-Incze, P., Skakalova, V., Biro, L. P., Klitzing, K. V., and Smet, J. H. (2010). Raman scattering at pure graphene zigzag edges. **Nano letters**. 10(11): 4544-4548.

Kresse, G., and Furthmüller, J. (1996). Efficient iterative schemes for ab initio total-energy calculations using a plane-wave basis set. **Physical review B**. 54(16): 11169.

Li, H., Zhou, X., Nummy, T., Zhang, J., Pardo, V., Pickett, W. E., Mitchell, J. F., and Dessau, D. S. (2017). Fermiology and electron dynamics of trilayer nickelate $\text{La}_4\text{Ni}_3\text{O}_{10}$. **Nature communications** 8(1): 1-7.

Li, Y., Tantiwanichapan, K., Swan, A. K., and Paiella, R. (2020). Graphene plasmonic devices for terahertz optoelectronics. **Nanophotonics** 9(7): 1901-1920.

Low, T., and Phaedon A. (2014). Graphene plasmonics for terahertz to mid-infrared applications. **ACS nano**. 8(2): 1086-1101.

- Luk'yanchuk, I. A., and Kopelevich, Y. (2006). Dirac and normal fermions in graphite and graphene: Implications of the quantum Hall effect. **Physical review letters**. 97(25): 256801.
- Mak, K. F., Lee, C., Hone, J., Shan, J., and Heinz, T. F. (2010). Atomically thin MoS₂: a new direct-gap semiconductor. **Physical review letters**. 105(13): 136805.
- Murali, B., Kolli, H. K., Yin, J., Ketavath, R., Bakr, O. M., and Mohammed, O. F. (2019). Single crystals: the next big wave of perovskite optoelectronics. **ACS Materials Letters**. 2(2): 184-214.
- Neder, V., Luxembourg, S. L., and Polman, A. (2017). Efficient colored silicon solar modules using integrated resonant dielectric nanoscatterers. **Applied Physics Letters**. 111(7): 073902.
- Neu, E., Appel, P., Ganzhorn, M., Miguel-Sánchez, J., Lesik, M., Mille, V., Jacques, V., Tallaire, A., Achard, J., and Maletinsky, P. (2014). Photonic nano-structures on (111) -oriented diamond. **Applied Physics Letters**. 104(15): 153108.
- Ni, Z. H., Yu, T., Lu, Y. H., Wang, Y. Y., Feng, Y. P., and Shen, Z. X. (2008). Uniaxial strain on graphene: Raman spectroscopy study and band-gap opening. **ACS nano**. 2(11): 2301-2305.
- Novoselov, K. S., Geim, A. K., Morozov, S. V., Jiang, D., Katsnelson, M. I., Grigorieva, I. V., Dubonos, S. V., and Firsov, A. A. (2005a). Two-dimensional gas of massless Dirac fermions in graphene. **Nature**. 438: 197.

- Novoselov, K. S., Geim, A. K., Morozov, S. V., Jiang, D., Katsnelson, M. I., Grigorieva, I., Dubonos, S. V., and Firsov, A. A. (2005). Two-dimensional gas of massless Dirac fermions in graphene. **Nature**. 438(7065): 197-200.
- Novoselov, K. S., Geim, A. K., Morozov, S. V., Jiang, D., Zhang, Y., Dubonos, S. V., Grigorieva, I. V., and Firsov, A. A. (2004). Electric field effect in atomically thin carbon films. **Science**. 306(5696): 666-669.
- Novoselov, K. S., Jiang, D., Schedin, F., Booth, T. J., Khotkevich, V. V., Morozov, S. V., and Geim, A. K. (2005). Two-dimensional atomic crystals. **The Proceedings of the National Academy of Sciences**. USA 102(30): 10451.
- Ohta, T., Bostwick, A., Seyller, T., Horn, K., and Rotenberg, E. (2006). Controlling the electronic structure of bilayer graphene. **Science**. 313(5789): 951-954.
- Orlita, M., Faugeras, C., Martinez, G., Maude, D. K., Sadowski, M. L., and Potemski, M. (2008). Dirac fermions at the H point of graphite: Magnetotransmission studies. **Physical review letters**. 100(13): 136403.
- Peng, J., Gao, W., Gupta, B. K., Liu, Z., Romero-Aburto, R., Ge, L., Song, L., Alemany, L. B., Zhan X., Gao, G., Vithayathil, S. A., Kaiparettu, B. A., Marti, A. A., Hayashi, T., Zhu, J. J., and Pulickel, M. A. (2012). Graphene quantum dots derived from carbon fibers. **Nano letters**. 12(2): 844-849.
- Perdew, J. P., Burke, K., and Ernzerhof, M. (1996). Generalized gradient approximation made simple. **Physical review letters**. 77(18): 3865.

- Perumbilavil, S., Sankar, P., Priya Rose, T., and Philip, R. (2015). White light Z-scan measurements of ultrafast optical nonlinearity in reduced graphene oxide nanosheets in the 400–700 nm region. **Applied Physics Letters**. 107(5): 051104.
- Pina-Hernandez, C., Koshelev, A., Dhuey, S., Sassolini, S., Sainato, M., Cabrini, S., and Munechika, K. (2017). Nanoimprinted high-refractive index active photonic nanostructures based on quantum dots for visible light. **Scientific reports**. 7(1): 1-8.
- Plotzing, T., Winzer, T., Malic, E., Neumaier, D., Knorr, A., and Kurz, H. (2014). Experimental verification of carrier multiplication in graphene. **Nano letters**. 14(9): 5371-5375.
- Reyntjens, S., and Puers, R. (2001). A review of focused ion beam applications in microsystem technology. **Journal of micromechanics and microengineering**. 11(4): 287.
- Ritter, K. A., and Lyding, J. W. (2009). The influence of edge structure on the electronic properties of graphene quantum dots and nanoribbons. **Nature materials**. 8(3): 235-242.
- Rodriguez, R. D., Khan, Z., Ma, B., Mukherjee, A., Meszmer, P., Kalbacova, J., Garratt, E., Shah, H., Heilmann, J., Walker, A. R. H., Wunderle, B., Sheremet, E., Hietschold, M., and Zahn, D. R. (2019). Ion-Induced Defects in Graphite: A Combined Kelvin Probe and Raman Microscopy Investigation. **Physica status solidi (a)**. 216(19): 1900055.

- Roldán, R., Castellanos-Gomez, A., Cappelluti, E., and Guinea, F. (2015). Strain engineering in semiconducting two-dimensional crystals. **Journal of Physics: Condensed Matter**. 27(31): 313201.
- Sato, K., Saito, R., Oyama, Y., Jiang, J., Cancado, L. G., Pimenta, M. A., JoribGe, A., Samsonidzec, G., Dresselhaus, G., and Dresselhaus, M. S. (2006). D-band Raman intensity of graphitic materials as a function of laser energy and crystallite size. **Chemical physics letters**. 427(1-3): 117-121.
- Shimatani, M., Fukushima, S., Okuda, S., and Ogawa, S. (2020). High-performance graphene/InSb heterojunction photodetectors for high-resolution mid-infrared image sensors. **Applied Physics Letters**. 117(17): 173102.
- Sk, M. A., Ananthanarayanan, A., Huang, L., Lim, K. H., and Chen, P. (2014). Revealing the tunable photoluminescence properties of graphene quantum dots. **Journal of Materials Chemistry C**. 2(34): 6954-6960.
- Tantiwanichapan, K., Wang, X., Durmaz, H., Li, Y., Swan, A. K., and Paiella, R. (2017). Graphene terahertz plasmons: A combined transmission spectroscopy and Raman microscopy study. **ACS Photonics**. 4(8): 2011-2017.
- Tassin, P., Koschny, T., and Soukoulis, C. M. (2013). Graphene for terahertz applications. **Science**. 341(6146): 620-621.
- Thiyagarajan, K., Ananth, A., Saravanakumar, B., Mok, Y. S., and Kim, S. J. (2015). Defect-induced metallic-to-semiconducting transition in multilayer graphene. **RSC advances**. 5(22): 16821-16827.

- Torben, W., Knorr, A., and Malic E. (2010) Carrier multiplication in graphene. **Nano letters**. 10.12: 4839-4843.
- Trauzettel, B., Bulaev, D. V., Loss, D., and Burkard, G. (2007). Spin qubits in graphene quantum dots. **Nature Physics**. 3(3): 192-196.
- Tuinstra, F., and Koenig, J. L. (1970). Raman spectrum of graphite. **The Journal of chemical physics**. 53(3): 1126-1130.
- Wang, Y., Kalytchuk, S., Zhang, Y., Shi, H., Kershaw, S. V., and Rogach, A. L. (2014). Thickness-dependent full-color emission tunability in a flexible carbon dot ionogel. **The journal of physical chemistry letters**. 5(8): 1412-1420.
- Wang, Y., Li, Y., Yan, Y., Xu, J., Guan, B., Wang, Q., Li, J., and Yu, J. (2013). Luminescent carbon dots in a new magnesium aluminophosphate zeolite. **Chemical Communications**. 49(79): 9006-9008.
- Winzer, T., Knorr, A., and Malic, E. (2010). Carrier multiplication in graphene. **Nano letters**. 10(12): 4839-4843.
- Wong, J. H., Wu, B. R., and Lin, M. F. (2012). Strain effect on the electronic properties of single layer and bilayer graphene. **The Journal of Physical Chemistry C**. 116(14): 8271-8277.
- Yoshida, T., Ideta, S. I., Shimojima, T., Malaeb, W., Shinada, K., Suzuki, H., Nishi, I., Fujimori, A., Ishizaka, K., Shin, S., Nakashima, Y., Anzai, H., Arita, M., Ino, A., Namatame, H., Taniguchi, M., Kumigashira, H., Ono, K., Kasahara, S., Shibauchi, T., Terashima, T., Matsuda, Y., Nakajima, M., Uchida, S., Tomioka,

- Y., Ito, T., Kihou, K., Lee, C. H., Iyo, A., Eisaki, H., Ikeda, H., Arita, R., Saito, T., Onari S., and Kontani, H. (2014). Anisotropy of the superconducting gap in the iron-based superconductor $\text{BaFe}_2(\text{As}_{1-x}\text{P}_x)_2$. **Scientific reports**. 4(1): 1-6.
- Zhang, W. (2014). Voltage-driven spintronic logic gates in graphene nanoribbons. **Scientific reports**. 4: 6320.
- Zhang, X., Dong, H., and Hu, W. (2018). Organic semiconductor single crystals for electronics and photonics. **Advanced Materials**. 30(44): 1801048.
- Zhang, X., Xin, J., and Ding, F. (2013). The edges of graphene. **Nanoscale**. 5(7): 2556-2569.
- Zhang, Y., Tan, Y. W., Stormer, H. L., and Kim, P. (2005). Experimental observation of the quantum Hall effect and Berry's phase in graphene. **Nature**. 438(7065): 201-204.
- Zhang, Y., Tang, T. T., Girit, C., Hao, Z., Martin, M. C., Zettl, A., Michael F. Crommie, M. F., Y. Ron Shen Y. R., and Wang, F. (2009). Direct observation of a widely tunable bandgap in bilayer graphene. **Nature**. 459(7248): 820-823.
- Zhou, S. Y., Gweon, G. H., Fedorov, A. V., First, P. D., De Heer, W. A., Lee, D. H., Guinea, F., Castro Neto, A. H., and Lanzara, A. (2007). Substrate-induced bandgap opening in epitaxial graphene. **Nature materials**. 6(10): 770-775.

Zhou, S. Y., Gweon, G. H., Spataru, C. D., Graf, J., Lee, D. H., Louie, S. G., and Lanzara, A. (2005). Coexistence of sharp quasiparticle dispersions and disorder features in graphite. **Physical Review B**. 71(16): 161403.



CURRICULUM VITAE

Sujinda Chaiyachad

Tel: (66) 84-7963-909 Email: sujinda.chaiyachad@gmail.com



Education:

- 2015 - 2021: Doctor of Philosophy (Physics) Suranaree University of Technology, Nakhon Ratchasima, Thailand
- 2011 - 2015: Bachelor of Science (Physics) Khon Kaen University, Khon Kaen, Thailand (1st class honors in Physics)

Honors And Awards:

- *Recipient*, Scholarship from the Development and Promotion of Science and Technology Talents Project, Thai government, 2011 -2021

Publication:

- Eknapakul, T., Fongkaew, I., Siriroj, S., Jindata, W., **Chaiyachad, S.**, Mo, S. K., ... & Meevasana, W. (2018). Direct observation of strain-induced orbital valence band splitting in HfSe₂ by sodium intercalation. *Physical Review B*, 97(20), 201104.
- Jaiban, P., Lu, M. H., Eknapakul, T., **Chaiyachad, S.**, Yao, S. H., Pisitpipathsin, N., ... & Meevasana, W. (2020). Spectral weight reduction of two-dimensional electron gases at oxide surfaces across the ferroelectric transition. *Scientific reports*, 10(1), 1-7.
- Jindata, W., Hantanasirisakul, K., Eknapakul, T., Denlinger, J. D., Sangphet, S., **Chaiyachad, S.**, ... & Meevasana, W. (2021). Spectroscopic signature of negative electronic compressibility from the Ti core-level of titanium carbonitride MXene. *Applied Physics Reviews*, 8(2), 021401.